The Dynamics of the Beaufort Gyre

by

Elizabeth Webb

A thesis
presented to the University of Waterloo
in fulfillment of the
thesis requirement for the degree of
Master of Mathematics
in
Applied Mathematics (Water)

Waterloo, Ontario, Canada, 2020

Author's Declaration

I hereby declare that I am the sole author of this thesis. This is a true copy of the thesis, including any required final revisions, as accepted by my examiners.

I understand that my thesis may be made electronically available to the public.

Abstract

The Beaufort gyre is located in the Canadian Arctic basin and is responsible for the dominant circulation of the Beaufort Sea. Currently, the gyre flows in an anti-cyclonic direction, which leads to the deflection of fresh water from melting sea ice into the centre due to the Coriolis force. However, every 5 - 7 years it has been observed to reverse direction and release the collected fresh water into Transpolar Drift, towards the Northern Atlantic Ocean. The last recorded reversal was over 20 years ago, and the Beaufort gyre now holds as much fresh water as all the Great Lakes combined. When the next reversal happens, it is predicted that the fresh water will be released and then act as a thick, cold blanket over the Northern Atlantic Ocean, preventing heat transfer to the atmosphere, and greatly affecting the European climate and fisheries.

The research in this thesis aims to understand the structure of the Beaufort gyre and how it might destabilize and give rise to eddies. Eddies are known to be very effective in mixing the deep Arctic ocean water with the cold fresh surface water, which could lead to the increased melting of the floating sea ice. In this work we develop numerical tools that can be used to study both the classical wind-driven gyre problem, and also an idealized Beaufort gyre. We use the reduced gravity, Quasi-Geostrophic model, which accounts for the effects of the rotation of earth, wind forcing, bottom drag and lateral viscosity. The solutions are computed using Firedrake, a finite element method library, and we examine how the structure of the steady solution depends on varying values of bottom drag, the beta effect and stratification. Subsequently, we investigate the linear stability of the gyre. Unfortunately, we were not able to simulate winds that are as strong as are observed and as a result did not simulate any instabilities, but the tools have been established for future research.

Acknowledgements

There are so many people that I would like to acknowledge and thank on this page. Most importantly, I'd like to thank my supervisor, Francis Poulin, for giving me this amazing opportunity to learn about the Beaufort gyre, and for the constant support, patience, and encouragement. You went above and beyond my expectations of a supervisor and I am extremely grateful. I would also like to thank Marek Stastna and Michael Waite, as well as Francis, for taking the time to read through my thesis and provide constructive feedback. The mentorship is truly appreciated and I am very thankful for this learning opportunity.

Thank you to Sarah Walsh, and other members of the Applied Math department who put up with my nonsense and made the windowless offices barely noticeable! I'd also like to thank my other friends who supported me throughout this process, and who were accepting of my absence for sometimes months at a time. I hope you will accept my thesis as my apology; if not to read, perhaps you can use my solution plots as wall decor.

Thank you to my high school math teachers. I don't know if I would have continued if not for Shawn Chen, David Bocknek, and (last but not least) Murray Miller. You challenged me when I temporarily lost interest in school, and called me out when I wasn't putting in the proper effort. You make a huge impact on students' lives and I hope you know how grateful I am to have had such amazing teachers.

Thank you to my family. My dad, for keeping my standards high and for reminding me that graduate school is sometimes hard but I am fully capable of pushing through it. My mom, for always calling to check on me, and then for continuing to call even after I lost my temper. Thank you to my sister for trying to understand my research and for telling all your friends about it. Now you can link them to my thesis!

Finally, thank you to George for being there every step of the way. From studying calculus together in high school, to helping me structure my master's thesis. It has been a long journey and it would not have been the same without you.

Dedication

To my Aunt Betty,
who passed in the early stages of this thesis.

Table of Contents

List of Tables

List of Figures

Chapter 1

Introduction

1.1 The Beaufort Gyre

Oceans are vital to life on Earth; they play a major role in the distribution of heat, nutrients and salinity across the globe [44]. The large-scale circulation of the oceans are dominated by wind-driven gyres, which consist of slow rotational motions in the interior and frequently have a strong jet near the western boundary. These so-called western boundary currents are due to the curvature of Earth, the winds that blow above the oceans and dissipation that acts on smaller scales. However, there are examples of gyres with very different dynamics in that they do not exhibit western intensification, such as the Beaufort gyre.

This thesis focuses on the Beaufort gyre (BG), which is located in the Canadian Arctic basin, north of the Yukon territory, refer to [42]. The Arctic is undeniably a topic of interest in relation to climate change. In recent years, melting sea ice has become a constant in the daily news; the heating of the Arctic is felt everywhere. The Beaufort gyre catches and stores much of the fresh water from the melting sea ice, as well as run off from the Mackenzie River and Bering Strait [32]. Currently the Beaufort gyre is rotating in a clockwise (anti-cyclonic) direction, and it has been observed to transport oceanic properties, such as fresh water, to the centre of the gyre.

Historically, the Beaufort gyre has been recorded to reverse direction on average every 5 to 7 years. This reversal results in the release of fresh water into the Transpolar Drift, which is then sent towards the Northern Atlantic Ocean [4]. However, it has been over 20 years since the last recorded reversal and the gyre reached a maximum of more than $22,000$ km^3 of fresh water in 2015, which is similar to the amount of water in all the Great

Lakes combined [1][15]. Due to a difference in densities, the fresh water sits on top of the salty Arctic water, with much of the fresh water in the centre of the gyre [8]. The fresh water is very cold, as it originates from the frozen sea ice, and therefore acts as a barrier between the floating ice and the salty warmer water below [39]. From this perspective, the Beaufort gyre's fresh water content extends the life of sea ice by protecting it from the warmer waters.

The Beaufort gyre system holds the fate of the fresh water content in the Arctic Ocean [39][31]. The exact consequences of a reversal are unknown, however we may look at the results of previous reversals as an indication of what may come. In the past, there have been several occurrences of large amounts of fresh water being released into the Atlantic Ocean, which may be referred to as a Great Salinity Anomaly (GSA) [31] [2]. In 1968, a GSA was identified in the Greenland Sea, which then circulated in the Atlantic subpolar gyre for over 14 years, reaching depths as far as 500 m below the surface [7]. Studies have been done to locate the origin of this specific GSA, many of which point to the BG [13] [7]. If the BG releases 5% of the current reservoir, the world may see similar results as the GSA of the late 60's, which has been suggested to have prevented convection in the Labrador Sea [13] [15]. The GSA of the 90's has also been attributed to the reversal of the BG, which led to several of Europe's harshest winters on record [2][15]. Based on these past events, it is predicted for the fresh water to be released into the Northern Atlantic ocean and act as a thick, cold blanket which will reduce heat transfer between the ocean and the atmosphere [15]. This blanket is expected to cause a temporary cooling effect over the climate of Western Europe, as well as negatively affecting the European fisheries [15].

The Beaufort gyre demands the attention of scientists worldwide by having the largest reservoir of fresh water in the Arctic. As ice cover continues to melt, the water becomes more exposed to the wind forcing. The winds are able to transfer more and more momentum into the Beaufort gyre system, so the equilibrium state must also change. Meneghello et al. (2018) compared the terminal velocities of both an ice covered and free surface Beaufort gyre model [25]. In this work, they introduce the Ice-Ocean Governor, which describes the interaction of ice with the underlying ocean current. They argue the Ice-Ocean Governor will determine the equilibrium state of the Beaufort gyre, and the reduced ice coverage will lead to a faster moving gyre, and possibly lead to baroclinic instabilities. However, drifter data suggests eddies are present in the Beaufort gyre, which contribute to the transport of heat from the bottom of the ocean to the surface [18]. Doddridge et al. (2019) extended the Ice-Ocean Governor theory by investigating the balance between mesoscale eddies, wind and the Ice-Ocean Governor in reference to the evolution of the Beaufort gyre [8]. Their results indicate that mesoscale eddies should also be considered in the modelling of the Beaufort gyre, and emphasize the importance in understanding

mesoscale eddies, as well as the Ice-Ocean Governor.

The work done in this thesis aims to investigate two complimentary questions. First, what is the structure of the Beaufort gyre that can exist with a circular wind blowing above? Second, is this idealized solution unstable and if yes what kind of instabilities develop? We choose to model the Beaufort gyre using a highly idealized Quasi-Geostrophic (QG) model with a reduced gravity. Even though this model only allows for barotropic instabilities, this is a first step before investigating a multi-layer system, which is inherently more complicated. We use the finite element method to solve the linear steady equations, the nonlinear time dependent QG equations and the linear equations that describe the linear stability of the gyre.

To develop the tools needed to study the Beaufort gyre, we first look at the classical wind-driven gyre problem. The parameters used in to investigate the classical problem are from [30] and [17], who were able to generate a meandering western boundary current and subsequently eddies. Similar studies, such as [35] and [14], solve the steady, nonlinear time-dependent and linear stability models for a barotropic, sub-tropical wind driven gyre. However, these papers solved the nonlinear steady QG problem and varied the Reynolds number. The low Reynolds number solutions were very similar to the classical Stommel and Munk problems, but for higher Reynolds numbers, the steady solution looked like a Fofonoff mode. They also found that multiple solutions can occur. We instead focus on the linear steady solutions, and therefore assume that the basic state is in the lower Reynolds number regime. This is chosen in part because this is a simpler problem.

After studying the classical gyre, we apply these methods to an idealized Beaufort gyre with flat bathymetry and Gaussian wind forcing. Even though lateral eddy viscosity is bound to be important we choose to neglect this force and instead focus on bottom drag as the primary mechanism of dissipation for the Beaufort gyre. In the next section, we provide a brief introduction to geophysical fluid dynamics which is required in this work.

1.2 Geophysical Fluid Dynamics

Geophysical fluid dynamics (GFD) focuses on large scale flows on earth, and those found on other planets. There are two distinguishing attributes of GFD which puts it apart from other studies within the field of fluid dynamics: rotation and/or stratification [5]. Both play a significant role in the realm of GFD. We will begin by briefly discussing both rotation and stratification, as well as introduce some of the non-dimensional numbers used in this thesis.

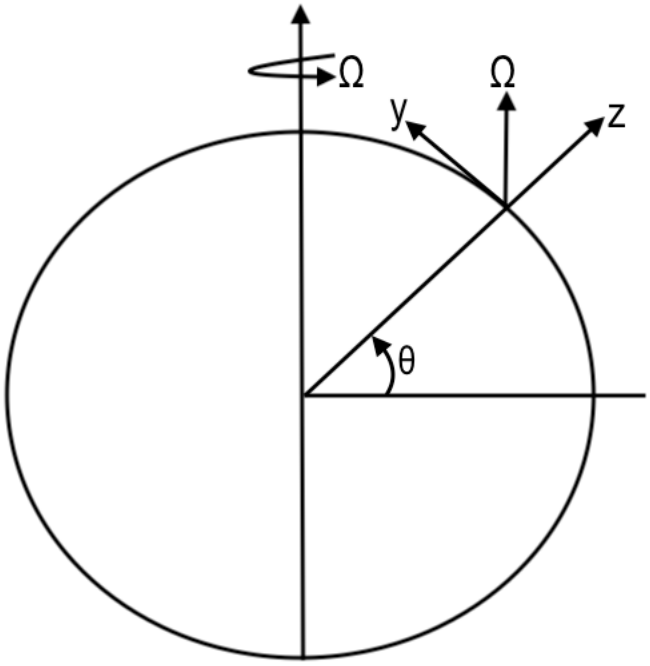

Figure 1.1: The angular velocity in Cartesian coordinates for a given latitude.

1.2.1 The Coriolis Force

As mentioned above, geophysical fluid dynamics encompasses flows for which the rotation of Earth is important. In these cases, we need to include the Coriolis term in our mathematical representations. The Coriolis effect is a result of a rotating spherical planet, where locations closer to the equator rotate faster than those away from the equator. The effect is responsible for the deflection of motion; in the northern hemisphere the motion is deflected to the right, and in the southern hemisphere, the motion is to the left. Mathematically, the contributions made by the rotating reference frame may be included by adding the Coriolis pseudo-force, denoted by $2\boldsymbol{\Omega} \times \mathbf{v}$, to the momentum equation, where $\boldsymbol{\Omega}$ is the angular velocity of Earth such that $\boldsymbol{\Omega} = \Omega\mathbf{k}$, and $\mathbf{v}$ is the three dimensional velocity vector [41] [19][5]. The derivation of the Coriolis term can be found in [19], [5] or [41]. By projecting the rotation vector in the northward and vertical directions, as shown in Figure 1.1, we

may obtain the angular velocity in Cartesian coordinates at a given latitude, θ:

$$\mathbf{\Omega} = (0, \Omega\cos\theta, \Omega\sin\theta). \tag{1.1}$$

Therefore, the Coriolis force may be written:

$$2\mathbf{\Omega} \times \mathbf{v} = (f^*w - fv, fu, -f^*u), \tag{1.2}$$

where we define $f = 2\Omega\sin\theta$ and $f^* = 2\Omega\cos\theta$ to be the traditional and non-traditional Coriolis parameters and θ is latitude [5]. In the northern hemisphere, the Coriolis parameter takes on a positive value, and a negative value in the southern hemisphere. The non-traditional Coriolis parameter is primarily of importance near the equator and since we are at high latitudes, we make the approximation $f^* \approx 0$, thereby making the traditional approximation [19].

The so-called f-plane model approximation makes the following approximation $f \approx f_0 = 2\Omega\sin\theta_0$. This is a reasonable model to use if the deviations in latitude are small. However, this assumption removes any western intensification in an oceanic gyre and is not appropriate for the variations in latitude that occur in the Beaufort Gyre. Alternatively, we may use the beta-plane model, where we take the the linear approximation, $f \approx (f_0 + \beta y)$, where $\beta = \frac{1}{a}\frac{\partial f}{\partial \theta} = (2\Omega\cos\theta_0)/a$, and a is the radius of Earth. The beta-plane model is required in the classical theory of wind-driven gyres, however higher orders may also be used. We restrict ourselves to a linear beta-plane in this thesis as this is the simplest and most conventional choice. Next, we will introduce the Rossby number which indicates the importance of the Coriolis force.

Rossby Number

It is useful to determine the relative importance of the different terms in the momentum balance. This requires estimating the order of magnitude of the different variables in the problem. One important parameter that frequently arises in GFD is the Rossby number, which may be obtained by estimating the relative importance of the inertial forces and the Coriolis forces. These terms written out are $(\mathbf{v}\cdot\nabla)\mathbf{v}$ and $\mathbf{f}\times\mathbf{v}$ and have scales U^2/L and fU respectively, where U is the typical velocity scale and L is the typical length scale. We define the Rossby number:

$$Ro = \frac{U}{fL}. \tag{1.3}$$

If the rotation of the Earth is insignificant, then the relative acceleration dominates resulting in a large Rossby number. However, if the rotational acceleration is very important

compared to the relative acceleration, then we obtain a very small Rossby number. For example, in oceanic gyres, the Rossby number is on the order of 0.01, indicating that rotation is very important [5]. If the Rossby number is small then the motion tends to be near geostrophic balance. This balance occurs when the Coriolis force dominates and is balanced with the pressure force. The collection of fresh water in the centre of the Beaufort gyre is a result of near geostrophic balance.

The Beaufort gyre has been observed to be in nearly geostrophic balance, where the Coriolis force deflects the motion inward and the pressure force is directed outwards, which is known as the Beaufort High. As the Beaufort gyre collects more and more fresh water, the sea level rises and begins to create a dome like structure, where the water continues to flow nearly along lines of constant pressure [1]. The collection of the fresh water on top of the Arctic water may be approximated by a stratified two layer model. Next we will discuss how the Burger number indicates the importance of stratification.

1.2.2 Stratification

Stratification is the natural layering that occurs due to differences in density. For example, in the Beaufort gyre, the salt water has a higher density, and thus sinks, allowing the fresh water to sit in the upper layers of the ocean. Similar to the Rossby number indicating the importance of rotation, the Froude number and the Burger number may indicate the importance of stratification.

The Froude Number and the Burger Number

The Froude number may be defined in multiple ways. In the context of a continuously stratified fluid, we introduce it as,

$$Fr = \frac{U}{NH}, \tag{1.4}$$

where H is the vertical length scale and N is the stratification frequency. The stratification frequency is also known as the Brunt-Väisälä (buoyancy) frequency and is defined such that $N^2 = -\frac{g}{\rho_0}\frac{d\rho}{dz}$, where g is the gravitational acceleration, ρ_0 is the reference density and $\frac{d\rho}{dz}$ is the vertical rate of change in density [5]. The Froude number is similar to the Rossby number in the sense that it is also a ratio of horizontal velocity to a frequency multiplied by a length scale. In this sense the Froude number is an indication of the importance of stratification. When $Fr \ll 1$, stratification is very important, and when $F \gg 1$ effects of stratification are negligible [5].

However, as mentioned above, the Froude number may be defined in other ways depending on the kind of stratification. In this work, which focuses on the top layer of a two layer model, we choose to use the Burger number which may be defined in terms of the Froude number. That is we define the Burger number by

$$Bu = \left(\frac{Ro}{Fr}\right)^2 = \left(\frac{L_d}{L}\right)^2, \tag{1.5}$$

where $L_d^2 = g'H/f^2$ is the Rossby radius of deformation, g' is the reduced gravity defined by $g' = g\frac{\rho_2-\rho_1}{\rho_2}$, g is the gravitational force, ρ_1 is the density of the top layer, ρ_2 is the density of the passive, bottom layer and L is the typical horizontal length scale. By assuming a small Rossby number, as done in the work here, a large Burger number signifies that stratification is very important and a small Burger number would suggest stratification is negligible. For example, the Burger number associated with the Beaufort gyre is on the order of 0.01, and thus suggests stratification does not play a significant role in the current modelling regime.

1.3 Thesis Format

The structure of this thesis is as follows. Chapter 2 is broken down into three subsections. The first subsection, 2.1, encompasses the necessary mathematical background leading up to the governing QG model. We begin with the equations of motion for a stratified, compressible fluid, then discuss the hydrostatic approximation and the Boussinesq approximation. This leads to deriving the single layer Shallow Water (SW) model, which assumes a homogeneous fluid in hydrostatic balance with a small aspect ratio. We conclude the subsection by presenting the non-dimensional the SW equations. In the second subsection, 2.2, we derive the governing models used in this thesis. To derive the QG model, we take an asymptotic expansion of the non-dimensional SW model in terms of the small Rossby number. By investigating the leading order and first order problems, we obtain an expression for the QG potential vorticity (PV). We then vertically integrate the non-dimensional QG equations for a stratified system and conclude with the wind-driven gyre model, also known as the Stommel/Munk Model. After this, we derive the boundary layer thicknesses that result from the Stommel model and the Munk model. We then present the dimensional governing equations and the necessary boundary conditions. The final subsection in Chapter 2, 2.3, derives the linear stability model, which is obtained by perturbing the basic state and linearizing. The linear stability model uses the same boundary conditions as stated in the second subsection, and models the growth of perturbations.

In Chapter 3, we present the numerical methods used to solve the governing models of Chapter 2. We begin by providing a brief introduction to the finite element method, and a breakdown of the notation. In the first subsection, 3.1 we derive the weak form needed in solving the steady model. In the second and third sections, 3.2 and 3.3, we derive the weak form necessary for the time dependent models and the linear stability model respectively, where we implement finite difference Backward Euler method for the time stepping part of the algorithm.

In Chapter 4 we present the results obtained by implementing the finite element method to the equations of Chapter 2 in the Firedrake library [10]. The chapter has been split into two different regimes: the classical wind driven gyre and the Beaufort gyre. Within each regime, we include a section on the parameters implemented, followed by the steady solutions, the nonlinear solutions and the linear stability solutions. The classical gyre, 4.1 uses a square domain and the parameters have been chosen to reproduce results from previous work done by [30] and [17]. We show the linear steady results of a shrinking western boundary current for a variety of values of bottom drag. After, we present the solutions of the nonlinear, time-dependent model, initialized with zero potential vorticity, and show it converges to the steady solution. We then present the results of another nonlinear, time-dependent simulation where we initialize the potential vorticity with the steady solution plus a small perturbation and watch how these perturbations evolve. We investigate the evolution of the perturbations in both nonlinear model and with the linear stability problem. We then apply the same solvers to the Beaufort gyre regime in 4.2 and analyze the solutions.

Lastly, in Chapter 5, we conclude and summarize our findings for the two investigations. Additionally, we present future direction of this work, which includes areas that may be improved on, as well as areas to which may be investigated further on this project.

Chapter 2

Governing Equations

This chapter outlines the necessary mathematical background for the physical models used in this thesis. The chapter starts with a section on the preliminary equations of motion, applies the hydrostatic approximation, the Boussinesq approximation and derives the shallow water (SW) model. The non-dimensional SW model is then used to derive the quasi-geostrophic (QG) model, and the Stommel/Munk model for wind-driven gyres [41]. The section concludes with the dimensional Stommel-Munk model and the boundary conditions. The final section in this chapter provides the derivation of the linear stability model, as well as a brief discussion of possible solutions. In Chapter 3, we present the numerical methods used to solve for the equations derived here.

2.1 Preliminary Equations

As most fluid dynamic stories begin, we present the equations of fluid motion. The continuity equation (2.1) states that the mass of a fluid element is conserved [41]. Equivalently, it says the compression or expansion of the fluid will result in a nonzero convergence or divergence [5]. The momentum equation (2.2) expresses Newton's second law, stating that the rate of change of a fluid element's momentum or velocity is proportional to the net forcing on the element [34]. The external forcing we consider are the Coriolis force and the pressure force. Lastly, the equation of state (2.3) relates the pressure with density, salinity and temperature, and is required for a closed system [5]. We present the conventional equation of state [5]. The continuity equation, momentum equation and equation of state

are for a compressible fluid:

$$\frac{\partial \rho}{\partial t} + \nabla \cdot (\rho \mathbf{v}) = 0, \tag{2.1}$$

$$\frac{\partial \mathbf{v}}{\partial t} + (\mathbf{v} \cdot \nabla)\mathbf{v} + \mathbf{f} \times \mathbf{v} = -\frac{1}{\rho}\nabla p - g\mathbf{k} + \nu \nabla^2 \mathbf{v}, \tag{2.2}$$

$$p = p(\rho, T, S). \tag{2.3}$$

We define the three dimensional velocity by $\mathbf{v} = (\mathbf{u}, w)$, and $\mathbf{f}$, ρ, p, g, ν T and S are the Coriolis parameter, density, pressure, gravitational acceleration, kinematic viscosity, temperature and salinity respectively. These equations, referred to as the Navier-Stokes equations, are the starting point to the governing model used in this work, however they require further simplifications prior to the model derivation [41]. It is worth noting that in large-scale flows, the viscosity term appears as it does in the above equation but ν is instead thought of an eddy viscosity, which parameterizes the effects of the small scales. We begin by applying the hydrostatic approximation.

2.1.1 The Hydrostatic Approximation

The hydrostatic approximation assumes that the system is in hydrostatic balance. That is, it assumes the vertical momentum equation reduces to a balance between the vertical pressure gradient and the gravitational force [19],

$$\frac{\partial p}{\partial z} = -\rho g. \tag{2.4}$$

The hydrostatic approximation is appropriate to most systems where the horizontal length scale is much larger than the vertical length scale, $H \ll L$, or equivalently a system with a small aspect ratio, $H/L \ll 1$ [41]. For the work done here, the small aspect ratio is satisfied given the focus is put on hundreds of metres in the vertical direction and on tens of kilometers or more in the horizontal domain [5]. Moreover, assuming a small aspect ratio results in a bound on the vertical velocity. We may find this by analyzing the scales of the the continuity equation for constant density:

$$\frac{\partial u}{\partial x} + \frac{\partial v}{\partial y} + \frac{\partial w}{\partial z} = 0, \tag{2.5}$$

$$\frac{U}{L} \qquad \frac{U}{L} \qquad \frac{W}{H} \tag{2.6}$$

where U and L are the typical velocity scale and length scale in the horizontal direction, and W and H are are the typical velocity scale and length scale in the vertical direction. Since the third term above must balance the sum of the first two, we obtain the following bound on the order of magnitude of the vertical velocity,

$$W = O\left(\frac{UH}{L}\right), \tag{2.7}$$

Therefore, an incompressible fluid with a small aspect ratio, $H/L \ll 1$ [5] necessarily has a weaker vertical velocity when compared to the horizontal: $W \ll U$ [5].

The next approximation that will be discussed is the Boussinesq approximation.

2.1.2 The Boussinesq Approximation

As equation 2.3 suggests, density is related to pressure, temperature and salinity. Pressure may vary significantly due the natural stratification in the Earth's oceans, however, the density variations are quite small. The mean density of the worlds oceans is 1028 $kg\ m^{-3}$ and density variations are less than 5 percent of that, whether it be at the ocean surface or the bottom of the deepest ocean [19] [41]. The Boussinesq approximation exploits the fact that the deviations from the mean density are small and decomposes the total density as follows,

$$\rho = \rho_0 + \rho'(x, y, z, t), \tag{2.8}$$

where ρ_0 is the mean density and $\rho'(x, y, z, t)$ is a perturbation of much smaller amplitude, $|\rho'| \ll \rho_0$ [5]. The derivation of this approximation then proceeds with substituting equation 2.8 into the governing equations and looking at the balance of terms. The details are not shown here but the interested reader may find the full substitution and simplification in [41]; we provide the resulting equations.

Below are the continuity and momentum equations for an inviscid fluid, under the Boussinesq approximation, as well as the energy (buoyancy) equation:

$$\nabla \cdot \mathbf{v} = 0, \tag{2.9}$$

$$\frac{D\mathbf{v}}{Dt} + \mathbf{f} \times \mathbf{v} = -\frac{1}{\rho_0}\nabla p' + b\hat{k}, \tag{2.10}$$

$$\frac{Db}{Dt} = \dot{b}. \tag{2.11}$$

We have taken $p = p_0 + p'(x, y, z, t)$, $b = -g\rho'/\rho_0$, and $\dot{b} = g\beta_T \dot{Q}/c_p$ such that β_T, $\dot{Q}$ and c_p the coefficient of expansion due to temperature, the rate of heating, and the heat capacity at constant pressure respectively. These equations together form a closed system, known as the simple Boussinesq equations [41].

In summary, the Boussinesq approximation assumes the perturbation of density is negligible except in the buoyancy term [5]. Compressible effects are negligible when the Mach number U/c, is less than 0.3, where U is the typical flow speed and c is the speed of sound through the material [19]. The speed of sound through water is approximately $c = 1470$ m s^{-1} and the achievable typical flow speeds are much smaller than this, making it a common approximation in water [19].

The hydrostatic approximation and the Boussinesq approximation have significantly simplified the governing equations, but we continue to simplify. We will now look to derive the SW model which begins with a homogeneous fluid in hydrostatic balance.

2.1.3 The Shallow Water Model

The single layer SW model has been very useful in studying both atmospheric and oceanic dynamics [41]. The two dimensional set-up is provided in Figure 2.1. We take H to be the constant mean height of the water column, η the surface perturbation above the mean and $h(x, y)$ the total height such that $h(x, y) = H + \eta(x, y)$. It is bounded below by a rigid, flat surface, and above by a free surface with negligible inertia. The SW model is one of the simplest models, that assumes an inviscid, homogeneous fluid in hydrostatic balance with a small aspect ratio [41]. As discussed in Section 2.1.1, the small aspect ratio allows for the neglecting of the internal vertical motion, which is referred to as a barotropic flow [19][5]. We now begin deriving the SW model, which will depend on the horizontal velocity $\mathbf{u} = (u, v)$ and the total depth of the fluid, h. Note that the vertical velocity need not be zero and stretching and contraction can occur in the vertical direction.

Momentum Equation

To obtain the SW momentum equation, we begin with the equation for hydrostatic balance, equation 2.4. We then integrate from the bottom, $z = 0$ to the ocean surface, $z = H + \eta(x, y)$. Assuming the pressure is negligible at the surface, we obtain the following expression for pressure:

$$p(x, y, z) = \rho g(H + \eta(x, y)). \tag{2.12}$$

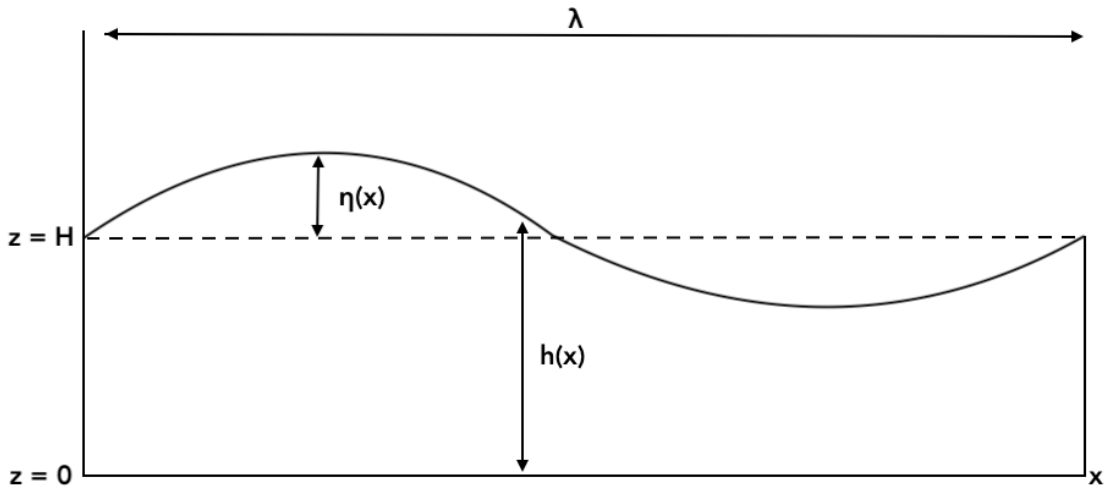

Figure 2.1: The geometry of the SW model where H is the constant mean depth, $\eta(x)$ is the surface deformation, and $h(x)$ is the total depth such that $h(x) = H + \eta(x)$. The wavelength is represented by λ, which is much larger than the mean depth, satisfying the small aspect ratio.

We then substitute this into the pressure term of the momentum equation and find $\nabla p = \rho g \nabla \eta$ [41]. The resulting SW momentum equation is shown in equation 2.16.

Continuity Equation

Similar to the SW momentum equation, the SW continuity equation is obtained by integrating in the vertical direction:

$$(H+\eta)\frac{\partial u}{\partial x} + (H+\eta)\frac{\partial v}{dy} + w(H+\eta) + w(0) = 0. \tag{2.13}$$

The vertical velocity at the bottom is zero if the bottom is flat, and at the top it is equal to the free surface velocity, Dh/Dt [41]. Applying these substitutions, as well as letting $h(x,y) = H + \eta(x,y)$:

$$h\frac{\partial u}{\partial x} + h\frac{\partial v}{dy} + \frac{Dh}{Dt} = 0. \tag{2.14}$$

The final SW continuity equation is shown in equation 2.15. Together with the momentum equation completes the SW model:

Shallow Water Model

$$\frac{Dh}{Dt} + h\nabla \cdot (\mathbf{u}) = 0, \tag{2.15}$$

$$\frac{D\mathbf{u}}{Dt} + \mathbf{f} \times \mathbf{u} = -g\nabla\eta. \tag{2.16}$$

We could have written the right hand side of the momentum equation in terms of h instead of η however for non-dimensional purposes, we choose to keep the SW equations as stated above [41]. Additionally, up to this point, the Coriolis term has remained without assumptions or simplifications. However, moving forward the beta plane approximation will be used as discussed in Section 1.2.1, such that $\mathbf{f} = (f_0 + \beta y)\mathbf{k}$, where f_0 is the reference Coriolis parameter, and β is the rate of change in Coriolis parameter.

Non-Dimensional Shallow Water Equations

The model used in this work is derived using the non-dimensional SW model. To obtain the non-dimensional form, variables are assumed to be the product of a non-dimensional variable (denoted with a hat) and a constant (denoted with a capital letter) which has the

units associated with the original variable [5]. The coordinate variables, the velocities and advective time scale are written as follows:

$$(x, y) = L(\hat{x}, \hat{y}), \tag{2.17}$$

$$(u, v) = U(\hat{u}, \hat{v}), \tag{2.18}$$

$$t = \frac{L}{U}\hat{t}. \tag{2.19}$$

Applying this to the beta plane approximation, and assuming $\beta = \frac{U}{L^2}\hat{\beta}$:

$$\mathbf{f} = f_0(1 + Ro\hat{\beta}\hat{y})\mathbf{k}, \tag{2.20}$$

where we define the Rossby number $Ro = U/Lf_0$. Equations 2.17 to 2.20, as well as $\eta = \mathcal{H}\hat{\eta}$ are substituted into the SW momentum equation, equation 2.16. Note, the typical vertical perturbation scale, $\mathcal{H}$, is currently unknown. After dividing by f_0U and substituting the Rossby number where applicable, the momentum equation becomes:

$$Ro\left(\frac{\partial\hat{\mathbf{u}}}{\partial\hat{t}}\right) + Ro(\hat{\mathbf{u}}\cdot\hat{\nabla}\hat{\mathbf{u}}) + (1 + Ro\hat{\beta}\hat{y})\mathbf{k}\times\hat{\mathbf{u}} = \left(\frac{-g\mathcal{H}}{L}\frac{1}{f_0U}\right)\hat{\nabla}\hat{\eta}. \tag{2.21}$$

Based on the right hand side, an appropriate choice of the typical vertical perturbation would be $\mathcal{H} = Lf_0U/g$, or equivalently, $\mathcal{H} = R_oL^2f^2/g$. The final non-dimensional SW momentum equation is seen in equation 2.24. Moving forward to obtain the non-dimensional continuity equation, we begin with the vertical height:

$$h = H\left(1 + Ro\frac{L^2}{L_d^2}\hat{\eta}\right), \tag{2.22}$$

where where we redefine slightly the Rossby radius of deformation in terms of the reduced gravity, $L_d^2 = g'H/f_0^2$.

Following a similar procedure as the momentum equation, and defining the Burger number, $Bu = L_d^2/L^2$, the final non-dimensional SW continuity equation is shown in equation 2.23:

Non-Dimensional Shallow Water Model

$$\left(\frac{Ro}{Bu}\right)\frac{D\hat{\eta}}{D\hat{t}} + \left[1 + \left(\frac{Ro}{Bu}\right)\hat{\eta}\right]\hat{\nabla}\cdot\hat{\mathbf{u}} = 0, \tag{2.23}$$

$$Ro\left(\frac{\partial\hat{\mathbf{u}}}{\partial\hat{t}} + (\hat{\mathbf{u}}\cdot\hat{\nabla})\hat{\mathbf{u}}\right) + (1 + Ro\hat{\beta}\hat{y})\mathbf{k}\times\hat{\mathbf{u}} = -\hat{\nabla}\hat{\eta}. \tag{2.24}$$

This will be the starting point in deriving the non-dimensional QG model in the next section. At the end of this chapter, we provide the dimensional model which includes a table of each parameter, including those presented here. Refer to Table 2.1.

2.2 Governing Model

2.2.1 The Quasi-Geostrophic Model

Thus far we have assumed a small aspect ratio, a beta plane approximation, and taken an advective time scale. We further assume the Rossby number is small and that the variations in the layer depth are small compared to the total depth. As discussed in Section 1.2, the former assumption is appropriate for most large scale flows in the oceans and atmosphere. The latter assumption is also often used for the large scales since surface waves have amplitudes that are typically on the order of centimeters to meters, while the total depth in the ocean is kilometers [41].

We will now derive the Quasi-Geostrophic (QG) model in the inviscid limit. We begin by considering the non-dimensional variables, $\hat{u}$, $\hat{v}$ and $\hat{\eta}$, and take their asymptotic expansions in terms of a small parameter given by the Rossby number:

$$\hat{u} = \hat{u}_0 + Ro\hat{u}_1 + \dots , \tag{2.25}$$
$$\hat{v} = \hat{v}_0 + Ro\hat{v}_1 + \dots , \tag{2.26}$$
$$\hat{\eta} = \hat{\eta}_0 + Ro\hat{\eta}_1 + \dots . \tag{2.27}$$

We will substitute these into the the SW continuity equation 2.23 and the SW momentum equation 2.24. We neglect $\mathcal{O}(Ro^2)$ and assume $Bu = \mathcal{O}(1)$ such that $\frac{Ro}{Bu} = \mathcal{O}(Ro)$:

$$\left(\frac{Ro}{Bu}\right)\frac{D(\hat{\eta}_0 + Ro\hat{\eta}_1)}{D\hat{t}} + \left[1 + \left(\frac{Ro}{Bu}\right)(\hat{\eta}_0 + Ro\hat{\eta}_1)\right]\hat{\nabla}\cdot(\hat{\mathbf{u}}_\mathbf{0} + Ro\hat{\mathbf{u}}_\mathbf{1}) = 0, \tag{2.28}$$

$$Ro\left[\frac{\partial(\hat{\mathbf{u}}_\mathbf{0} + Ro\hat{\mathbf{u}}_\mathbf{1})}{\partial\hat{t}} + ((\hat{\mathbf{u}}_\mathbf{0} + Ro\hat{\mathbf{u}}_\mathbf{1})\cdot\hat{\nabla})(\hat{\mathbf{u}}_\mathbf{0} + Ro\hat{\mathbf{u}}_\mathbf{1})\right] + (1 + Ro\hat{\beta}\hat{y})\mathbf{k}\times(\hat{\mathbf{u}}_\mathbf{0} + Ro\hat{\mathbf{u}}_\mathbf{1}) = -\hat{\nabla}(\eta_0 + Ro\hat{\eta}_1). \tag{2.29}$$

The associated leading order problem is obtained by neglecting $\mathcal{O}(Ro)$ and are given by:

$$\hat{\nabla} \cdot \hat{\mathbf{u}}_{\mathbf{0}} = 0, \tag{2.30}$$

$$\mathbf{k} \times \hat{\mathbf{u}}_0 = -\hat{\nabla}\hat{\eta}_0. \tag{2.31}$$

If we write the components of equation 2.31, and define the streamfunction as $\hat{\psi}_0 = g\hat{\eta}_0/\hat{f}_0$ we obtain the following relations:

$$\hat{u}_0 = -\frac{\partial \hat{\psi}_0}{\partial \hat{y}}, \qquad \hat{v}_0 = \frac{\partial \hat{\psi}_0}{\partial \hat{x}}. \tag{2.32}$$

If we cross differentiate 2.32, we find this is equivalent to the leading order continuity equation, equation 2.30.

To obtain a closed system, we proceed to the first order problem. The first order continuity and momentum equations are shown below respectively,

$$\frac{1}{Bu}\frac{D\hat{\eta}_0}{D\hat{t}} + \frac{\hat{\eta}_0}{Bu}\hat{\nabla} \cdot \hat{\mathbf{u}}_{\mathbf{0}} + \hat{\nabla} \cdot \hat{\mathbf{u}}_{\mathbf{1}} = 0, \tag{2.33}$$

$$\frac{\partial \hat{\mathbf{u}}_{\mathbf{0}}}{\partial \hat{t}} + (\hat{\mathbf{u}}_{\mathbf{0}} \cdot \hat{\nabla})\hat{\mathbf{u}}_{\mathbf{0}} + \hat{\beta}\hat{y}\mathbf{k} \times \hat{\mathbf{u}}_{\mathbf{0}} + \mathbf{k} \times \hat{\mathbf{u}}_{\mathbf{1}} = -\hat{\nabla}\hat{\eta}_1. \tag{2.34}$$

The vorticity equation may be obtained by taking the curl of the momentum equation, equation 2.34. Doing this and writing the vertical component of vorticity as $\hat{\zeta}_0 = \nabla^2\hat{\psi}_0$ yields the resulting vorticity equation:

$$\frac{\partial \hat{\zeta}_0}{\partial \hat{t}} + (\hat{\mathbf{u}}_0 \cdot \hat{\nabla})(\hat{\zeta}_0 + \hat{\beta}\hat{y}) = -\hat{\nabla} \cdot \hat{\mathbf{u}}_1. \tag{2.35}$$

We use equation 2.33 to substitute an expression for the first order velocity into equation 2.35 and rearrange to obtain:

$$\frac{\partial}{\partial \hat{t}}\left(\hat{\zeta}_0 - \frac{1}{Bu}\hat{\eta}_0\right) + (\hat{\mathbf{u}}_{\mathbf{0}} \cdot \hat{\nabla})\left(\hat{\zeta}_0 + \hat{\beta}\hat{y} - \frac{1}{Bu}\hat{\eta}_0\right) = 0. \tag{2.36}$$

If we wish to obtain an equation in terms of just the streamfunction, we may apply the definitions for the vertical component of vorticity, as well as the definition of stream function as previously stated:

$$\frac{\partial}{\partial \hat{t}}\left(\hat{\nabla}^2\hat{\psi}_0 - \frac{1}{Bu}\hat{\psi}_0\right) + (\hat{\mathbf{u}}_0 \cdot \hat{\nabla})\left(\hat{\nabla}^2\hat{\psi}_0 + \hat{\beta}\hat{y} - \frac{1}{Bu}\hat{\psi}_0\right) = 0. \tag{2.37}$$

Since $\hat{\beta}\hat{y}$ is independent of time we can combine terms and equation 2.37 may then be written as:

Non-Dimensional Quasi-Geostrophic Potential Vorticity

$$\frac{D_0}{D\hat{t}}\left(\hat{\nabla}^2\hat{\psi}_0 + \hat{\beta}\hat{y} - \frac{1}{Bu}\hat{\psi}_0\right) = 0. \tag{2.38}$$

The subscript on the material derivative indicates the associated advective velocity is that of the zeroth order problem. When the right hand side is equal to zero, it is said to be conservative. The conserved scalar, for which the material derivative acts on, is referred to as the shallow water quasi-geostrophic potential vorticity (SW QG PV) model or simply the QG model. The material derivative may also be written as $\frac{D}{Dt} = \frac{\partial}{\partial t} + J(\psi, \cdot)$. For long time and space scales, geophysical flows tend to be in near geostrophic state, making the QG equations a suitable choice for some investigations [5].

If we had considered external forces in the QG derivation, the governing equation is very similar and would be given by:

$$\frac{D}{D\hat{t}}\left(\hat{\nabla}^2\hat{\psi} + \hat{\beta}\hat{y} - \frac{1}{Bu}\hat{\psi}\right) = \frac{\partial\hat{w}}{\partial\hat{z}} + curl_z\frac{\partial\hat{\tau}}{\partial\hat{z}}, \tag{2.39}$$

where $curl_z$ is the vertical component of the standard curl such that $curl_z\mathbf{A} = \mathbf{k}\cdot\nabla\times\mathbf{A}$ and $\hat{\tau}$ is the non-dimensional kinematic stress due to winds. The curl of the wind stress forces the vorticity, however the wind stress itself forces the momentum. In dimensional form, the kinematic stress has units Nm^{-2}.

The derivation for the forced dissipative QG system will not be presented in detail, but an interested reader can find the derivation in most textbooks on geophysical fluid dynamics such as [41]. The vertical velocity term on the right hand side arises from the vertical component of the vorticity equation for a Boussinesq system, and has an associated scale of $W = RoUH/L$. In the next section, we will find this term does not contribute to the Stommel/Munk Model, which can be attributed to it being $\mathcal{O}(Ro)$.

2.2.2 The Stommel/Munk Model

We now have the ingredients necessary to begin the Stommel Model derivation. We consider the case when the Burger number goes to infinity. Equation 2.39 becomes:

$$\frac{D\hat{\zeta}}{D\hat{t}} + \hat{\beta}\hat{v} = \frac{\partial \hat{w}}{\partial \hat{z}} + curl_z \frac{\partial \hat{\tau}}{\partial \hat{z}}, \tag{2.40}$$

where we have chosen to write the first term in terms of ζ for simplicity. As a reminder, we have defined $\hat{\zeta}$, $\hat{\beta}$, $\hat{v}$, $\hat{w}$, $curl_z$, and $\hat{\tau}$ to be the vertical component of vorticity, the gradient of the Coriolis parameter, the meridional component of velocity, the vertical velocity, the vertical component of curl, and the kinematic stress respectively. By vertically integrating, we obtain:

$$\int_b^t \frac{D\hat{\zeta}}{D\hat{t}}\, dz + \hat{\beta} \int_b^t \hat{v}\, dz = [\hat{w}]_b^t + curl_z[\hat{\tau}]_b^t, \tag{2.41}$$

where t is for the top of the water column with a rigid lid, and b is the flat bottom surface. On the left hand side, we will represent the vertical integration by a bar above the variable. On the right hand side, the vertical velocity is zero at both the near rigid lid surface, and at the solid flat bottom, forcing the first term to vanish. As discussed in the previous section, this is expected due to the associated scale being $\mathcal{O}(Ro)$. After evaluating the second term on the right hand side, we are left with two terms: the forcing due to the winds above, and the frictional forcing due to friction at the bottom.

Dissipation is typically important at the bottom of the oceans, with wind forcing being important at the top. Instead of resolving these complex regions, it is common to introduce Ekman layers that parameterize the effects of these regions [41]. There are two Ekman layers of interest in regards to equation 2.41: one at the top, which is exposed to the frictional forces imposed by the wind, and one at the bottom exposed to the frictional forces imposed by the bottom solid boundary [5]. We parametrize the top stress due to wind forcing [41] as follows:

$$\hat{G}_{winds}(\hat{x}, \hat{y}) = curl_z \hat{\tau}_{top} = \hat{k} \cdot \hat{\nabla} \times \hat{\tau}.$$

It is important to note here, the wind stress, $\hat{\tau}$ forces the momentum. However, the wind forcing shown here, $\hat{G}_{winds}$ is the curl of the wind stress, which forces the vorticity. If we take $\hat{\tau} = -A\cos(\pi\hat{y})$, where A is some magnitude with units m s^{-2}, these winds will produce a single gyre. The kinematic wind stress that will produce a double gyre is given by $\hat{\tau} = -A\cos(2\pi\hat{y})$.

Similarly, we parametrize the bottom stress by linear drag and let $curl_z\hat{\tau}_b = \hat{r}\hat{\zeta}$. The final Stommel model is [37]:

$$\frac{D\bar{\hat{\zeta}}}{D\hat{t}} + \hat{\beta}\bar{\hat{v}} = \hat{G}_{winds}(\hat{x},\hat{y}) - r\bar{\hat{\zeta}}. \tag{2.42}$$

Alternatively, if lateral viscosity is considered in place of bottom drag, we obtain the Munk model:

$$\frac{D\bar{\hat{\zeta}}}{D\hat{t}} + \hat{\beta}\bar{\hat{v}} = \hat{G}_{winds}(\hat{x},\hat{y}) + \hat{\nu}\hat{\nabla}^2\bar{\hat{\zeta}}, \tag{2.43}$$

where $\hat{\nu}$ is the non-dimensional kinematic eddy viscosity [28][41][5]. The derivation of the viscosity term has been omitted, but may be found in classical textbooks, such as [5]. It has been suggested that the Munk model is more accurate for oceanic gyres due to the fact that the wind driven circulation remains in the upper portion of the ocean, making bottom drag insignificant [41].

If we consider both bottom drag and viscosity, we obtain the Stommel-Munk model, shown in equation 2.44. In this equation and in this work, we have reintroduced the Burger number that was present in equation 2.39. We do this by writing the model in terms of $\hat{q}$ instead of $\hat{\zeta}$, which we define by equation 2.45. These changes have been applied to the equation below, where we have also dropped bars over variables for simplicity:

Non-Dimensional Stommel-Munk Model

$$\frac{D\hat{q}}{D\hat{t}} + \hat{\beta}\hat{\sigma_x} = \hat{G}_{winds}(\hat{x},\hat{y}) - \hat{r}\hat{q} + \hat{\nu}\hat{\nabla}^2\hat{q}, \tag{2.44}$$

$$\hat{q} = \hat{\nabla}^2\hat{\psi} - \frac{1}{Bu}\hat{\psi}, \tag{2.45}$$

$$\hat{\sigma} = \hat{\nabla}\hat{\psi}. \tag{2.46}$$

We have additionally introduced a variable for orthogonal velocity, such that $\sigma = (\sigma_x, \sigma_y) = (v, -u)$. The reasoning for this choice is related to the finite element method which is presented in Chapter 3.

Steady, Linear Model

For the purpose of this work, we are interested in obtaining steady solutions for the linear dynamics. The steady state is useful in understanding the spatial structure of the gyre

and may be obtained by neglecting the time dependent terms that arise from the material derivative. The linear model is valid when the nonlinear term is much smaller than the rotational term. These terms scale by U^2/L^2 and βU respectively, and by comparison, the following is a requirement when using the linear model:

$$R_\beta = \frac{U}{\beta L^2} \ll 1, \tag{2.47}$$

where R_β is referred to as the Rossby Beta number. Given the parameters listed in Table 4.6 and 4.2, this requirement is satisfied for the work done in this thesis. Below we present the steady, linear model:

Non-Dimensional Steady Linear Stommel-Munk Model

$$\hat{\beta}\hat{\sigma}_x = \hat{G}_{winds} - \hat{r}\hat{q} + \hat{\nu}\hat{\nabla}^2\hat{q}, \tag{2.48}$$

$$\hat{q} = \hat{\nabla}^2\hat{\psi} - \frac{1}{Bu}\hat{\psi}, \tag{2.49}$$

$$\hat{\sigma} = \hat{\nabla}\hat{\psi}. \tag{2.50}$$

In this work, we begin by solving the steady linear problem. Steady solutions may be stable or unstable depending on the parameters in the problem. An unstable basic state means that if it is perturbed, the perturbations will grow exponentially in time until they become sufficiently large to interact with the basic state. In Chapter 4, we show that solutions are asymptotically stable. For a randomized initial condition, the solution spins up to a wind-driven gyre which is very similar to the steady solution.

Western Boundary Layer Thickness

As we will show in Chapter 4, oceanic gyres with a non-zero beta are asymmetric in the zonal direction. Interestingly, the circulation always tends towards one with a western boundary current regardless of the direction of the winds, local topography or hemisphere [11]. Stommel (1948) [37] was the first to investigate this and described the phenomena as a 'westward crowding of streamlines'. The thickness of the western boundary is dependent on the choice of dissipation. It is referred to as a Stommel layer for dissipation in the form of bottom drag, and the Munk layer for dissipation in the form of lateral viscosity [37][28]. To obtain the Stommel layer, or the Munk layer, we analyze the scaling of the governing

model equation 2.44. Using Table 2.1, the right hand side can written as,

$$\frac{Dq}{Dt} + \beta\sigma_x = G_{winds} \; - \; rq \; + \; \nu\nabla^2 q, \tag{2.51}$$

$$\frac{U^2}{L^2} \qquad \beta U \qquad \frac{U^2}{L^2} \qquad \frac{rU}{L_S} \qquad \frac{\nu U}{L_M^3} \tag{2.52}$$

where we define L_s to be the typical length of the Stommel boundary layer, and L_M to be the typical length of the Munk boundary layer. If we assume the dominant balance is between the rotation and bottom drag, we obtain the Stommel layer thickness:

$$L_S = \frac{r}{\beta}. \tag{2.53}$$

Alternatively, as discussed above, some take the lateral viscosity to be more important than bottom drag, suggesting the dominant balance is between the rotation and the lateral viscosity. Making this choice, we obtain the Munk layer thickness similarly:

$$L_M = \left(\frac{\nu}{\beta}\right)^{1/3}. \tag{2.54}$$

Both equations 2.53 and 2.54 have been used to choose the bottom drag parameter and the lateral viscosity parameter in order to obtain a specific boundary thickness.

2.2.3 Dimensional Form

For completeness, this subsection provides the models in dimensional form. The work done in this thesis was strictly non-dimensional; however the conversion to dimensional is useful when comparing results to other works. To restore dimensions of the Stommel-Munk model, equation 2.44, the dimensional streamfunction and dimensional vertical component of vorticity are defined as $\psi = (g/f_0)\eta$, and $\zeta = \nabla^2\psi$ respectively. The resulting dimensional Stommel-Munk model becomes:

$$\frac{\partial q}{\partial t} + (\mathbf{u}\cdot\nabla)q + \beta v \;\; = \;\; G_{winds} - rq + \nu\nabla^2 q. \tag{2.55}$$

See Table 2.1 for the non-dimensional parameters, as well as the units associated with each term once in dimensional form.

Non-Dimensional to Dimensional		
Non-Dimensional Terms	Units	Dimensional
$(\hat{x}, \hat{y})$	m	$(x, y) = L(\hat{x}, \hat{y})$
$\hat{\mathbf{u}}$	$m\ s^{-1}$	$\mathbf{u} = U\hat{\mathbf{u}}$
$\hat{t}$	s	$t = \frac{L}{U}\hat{t}$
$\hat{\beta}$	$s^{-1}m^{-1}$	$\beta = \frac{U}{L^2}\hat{\beta}$
$\hat{\mathbf{f}}$	s^{-1}	$\mathbf{f} = f_0(1 + Ro\hat{\beta}\hat{y})\mathbf{k}$
$\hat{\eta}$	m	$\eta = (RoL^2f^2/g)\hat{\eta}$
$\hat{h}$	m	$h = H(1 + Ro\frac{L^2}{L_d^2}\hat{\eta})$
$\hat{\psi}$	m^2s^{-1}	$\psi = UL\hat{\psi}$
$\hat{\zeta}$	s^{-1}	$\zeta = \frac{U}{L}\hat{\zeta}$
$\hat{q}$	s^{-1}	$q = \frac{U}{L}\hat{q}$
$\hat{G}$	s^{-2}	$G = \frac{U^2}{L^2}\hat{G}$
$\hat{r}$	s^{-1}	$r = \frac{U}{L}\hat{r}$
$\hat{\nu}$	m^2s^{-1}	$\nu = UL\hat{\nu}$

Table 2.1: Summary of dimensional parameters.

2.2.4 Boundary Conditions

Here we describe the conditions at the boundary. These will be used in deriving the weak form and in the numerical implementation. Viscosity and diffusion appear in the terms of the highest differential order, and therefore influence the type and number of boundary conditions [41]. In this work, we consider a nonzero viscosity, which requires free-slip boundary condition be imposed in addition to no-normal flow boundary conditions, which are alwayw imposed.

No normal flow boundary conditions may be stated as,

$$\hat{\psi} = 0 \qquad \text{on} \quad \partial\Omega, \tag{2.56}$$

which states that flow may not pass through the solid boundary. The free-slip condition may be stated,

$$\hat{\nabla}\hat{q} \cdot \mathbf{n} = 0 \qquad \text{on} \quad \partial\Omega, \tag{2.57}$$

which means that the fluid can flow along a solid boundary. These boundary conditions are necessary in order to obtain a unique solution, and will also be applied to the linear stability model which will be introduced in the proceeding section.

2.3 Linear Stability Model

In this section we derive the linear stability problem for the wind-driven QG model. The resulting equation models the variations of the perturbations in time and will provide insight for the barotropic instabilities that may give rise to eddies in the system.

We begin by defining the basic state to be the solutions to the steady, linear model as described equation 2.48:

$$\psi_{st} = \Psi(x,y), \tag{2.58}$$
$$\vec{\sigma}_{st} = \vec{S}(x,y), \tag{2.59}$$
$$q_{st} = Q(x,y). \tag{2.60}$$

The basic state is dependent on the x and y coordinate in the domain. Next, we perturb the basic states by adding a small value which is dependent on both space and time,

$$\psi = \Psi(x,y) + \psi' x,y,t), \tag{2.61}$$
$$\vec{\sigma} = \vec{S}(x,y) + \vec{\sigma}'(x,y,t), \tag{2.62}$$
$$q = Q(x,y) + q'(x,y,t). \tag{2.63}$$

The perturbation is required to be significantly smaller than the basic state, such that

$$\|\psi'\|, \|\vec{\sigma}'\|, \|q'\| \ll 1 \quad \text{and} \quad \Psi, \vec{S}, Q = \mathcal{O}(1). \tag{2.64}$$

We now substitute these perturbed basic states into the nonlinear, non-dimensional governing equations (equations 2.44 to 2.46):

$$\frac{\partial q'}{\partial t} + \Big[\Big(\mathbf{k} \times (\vec{S} + \vec{\sigma}')\Big) \cdot \nabla\Big](Q + q') + \beta(S_x + \sigma'_x) = G_{winds} - r(Q + q') + \nu\nabla^2(Q + q'), \tag{2.65}$$

$$(Q + q') = \nabla^2(\Psi + \psi') - \frac{1}{Bu}(\Psi + \psi'), \tag{2.66}$$
$$(\vec{S} + \vec{\sigma}') = \nabla(\Psi + \psi'). \tag{2.67}$$

Last, we linearize equations 2.65 to 2.67 and obtain the linear stability model:

Non-Dimensional Linear Stability Model

$$\frac{\partial q'}{\partial t} + [(\mathbf{k} \times \vec{S}) \cdot \nabla]q' + [(\hat{k} \times \vec{\sigma}') \cdot \nabla]Q + \beta\partial_x\psi' = -rq' + \nu\nabla^2 q', \tag{2.68}$$
$$q' = \nabla^2\psi' - \frac{1}{Bu}\psi', \tag{2.69}$$
$$\sigma' = \nabla\psi'. \tag{2.70}$$

Equation 2.68 is very similar to the nonlinear QG model equation 2.44 except that we now have two advection terms instead of one: one is the advection of the perturbations by the mean flow and the second is the advection of the mean flow by the perturbations. As well note, there is no wind forcing term explicitly present in this model as that only affects the steady solution. If we study the evolution of perturbations in the linear stability model and the nonlinear model, they should agree very well when the amplitude of the perturbations are small. It is when the perturbations are sufficiently large in amplitude that they should deviate because then the nonlinear terms become more important.

In this work we will determine whether a steady solution is unstable by determining whether the perturbations grow exponentially in time in either of the two time-dependent codes. Alternatively, we could assume a normal mode (Fourier) decomposition in time of the form:

$$[\psi'(x,y,t), q'(x,y,t), \vec{\sigma}'(x,y,t)] = e^{-i\omega t}[\hat{\psi}(x,y), \hat{q}(x,y), \vec{\hat{\sigma}}(x,y)], \tag{2.71}$$

and then derive a two-dimensional eigenvalue problem that would need to be solved numerically. This approach is perfectly acceptable but is not the approach taken here. In this work, we monitor the norm of the linear stability solutions to identify instabilities in the model.

Chapter 3

Numerical Methods

This chapter includes a brief introduction to the finite element method, and presents the weak form derivations for the steady model, the time-dependent nonlinear model and the linear stability model, which were introduced in Chapter 2. These weak forms are necessary in order to implement the finite element method in the Firedrake Library [10]. The results are presented in the following chapter.

Below we restate the non-dimensional system of equations for the nonlinear Stommel-Munk model, where we have made the substitution $\vec{\sigma} = \nabla\psi = (\sigma_x, \sigma_y)$, such that $\vec{u} = \mathbf{k} \times \vec{\sigma} = (-\sigma_y, \sigma_x)$:

$$\partial_t q + ([\mathbf{k} \times \vec{\sigma}] \cdot \nabla)q + \beta\sigma_x = G_{winds} - rq + \nu\nabla^2 q, \tag{3.1}$$

$$q = \nabla^2\psi - \frac{1}{Bu}\psi, \tag{3.2}$$

$$\vec{\sigma} = \nabla\psi. \tag{3.3}$$

The variables we seek to solve for are ψ, $\vec{\sigma}$ and q. In the finite element method used here, these are referred to as the trial functions. We obtain our weak form by projecting each governing equation onto an associated test function, chosen from the appropriate function space. We label the test functions ϕ, $\vec{v}$ and p respectively. Both q and p belong to the discontinuous Lagrange space (DG) for conservation of enstrophy [27]. Second, $\vec{\sigma}$ and $\vec{v}$ belong to the Brezzi-Douglas-Marini (BDM) function space, which ensures a continuity in the normal direction across all elements. Last, ψ and ϕ belong to the Lagrange finite element function space (CG), in part because the streamfunction is obtained by inverting the associated Poisson problem and therefore can be taken as continuous.

The order of each space is associated with the order of the polynomials which directly affects the order of the finite element method. The CG space was set to be order 3, the

BDM space of order 2, and the DG space of order 1. The choice of spaces and degrees were inherited from previous work, such as [27]. The following sections derive the weak forms of each equation, which then needs to be discretized over the mesh. In particular, the domain, A, is decomposed into triangular elements, each denoted by K, which together yield T. To integrate a function, say f, over the domain, we must integrate f over each individual element, K, then sum the resultant over all elements,

$$\iint_A f dA = \sum_{K \epsilon T} \iint_K f dA. \tag{3.4}$$

This has been implemented in Firedrake [10].

3.1 Steady Model

We begin with the steady, nonlinear model. That is, we will begin with equations 3.1 to 3.3, and neglect time dependent terms. To find the weak form, we multiply each equation by an associated test function, p, ϕ, and v respectively, then integrate over each element K that exists in the domain, T:

$$\sum_{K \epsilon T} \iint_K \Big(([\hat{k} \times \vec{\sigma}] \cdot \nabla) q + \beta \sigma_x \Big) p \; dA = \sum_{K \epsilon T} \iint_K \Big(G_{winds} - rq + \nu \nabla^2 q \Big) p \; dA, \tag{3.5}$$

$$\sum_{K \epsilon T} \iint_K q \phi \; dA = \sum_{K \epsilon T} \iint_K \Big(\nabla^2 \psi - \frac{1}{Bu} \psi \Big) \phi \; dA, \tag{3.6}$$

$$\sum_{K \epsilon T} \iint_K \vec{\sigma} v \; dA = \sum_{K \epsilon T} \iint_K \Big(\nabla \psi \Big) v \; dA. \tag{3.7}$$

Next we apply integration by parts and apply the divergence theorem to the appropriate terms. Terms evaluated on the boundary have been combined on the right hand side:

$$\sum_{K\epsilon T}\iint_K \Big[-\nabla p\cdot(\hat{k}\times\vec{\sigma})q+\beta\sigma_x p - G_{winds}p + rqp + \nu\nabla p\cdot\nabla q\Big]\, dA = \tag{3.8}$$

$$\sum_{K\epsilon T}\oint_{\partial K}\Big[-pq(\hat{k}\times\vec{\sigma})\cdot\hat{n}+\nu p\nabla q\cdot\hat{n}\Big]\, ds, \tag{3.9}$$

$$\sum_{K\epsilon T}\iint_K \Big[q\phi+\nabla\phi\cdot\vec{\sigma}+\frac{1}{Bu}\psi\phi\Big]\, dA = \sum_{K\epsilon T}\oint_{\partial K}\phi\vec{\sigma}\cdot\hat{n}\, ds, \tag{3.10}$$

$$\sum_{K\epsilon T}\iint_K \Big[\vec{v}\cdot\vec{\sigma}+\psi\nabla\cdot\vec{v}\Big]\, dA = \sum_{K\epsilon T}\oint_{\partial K}\psi\vec{v}\cdot\hat{n}\, ds. \tag{3.11}$$

Last, we apply the boundary conditions as presented in Section 2.2.4 to the terms on the right hand side and conclude with the weak system of equations:

$$\sum_{K\epsilon T}\iint_K \Big[\beta\sigma_x p - G_{winds}p + rqp + \nu\nabla p\cdot\nabla q - \nabla p\cdot(\hat{k}\times\vec{\sigma})q\Big]\, dA = 0, \tag{3.12}$$

$$\sum_{K\epsilon T}\iint_K \Big[q\phi+\nabla\phi\cdot\vec{\sigma}+\frac{1}{Bu}\psi\phi\Big]\, dA = 0, \tag{3.13}$$

$$\sum_{K\epsilon T}\iint_K \Big[\vec{\sigma}\cdot\vec{v}+\psi\nabla\cdot\vec{v}\Big]\, dA = 0. \tag{3.14}$$

This concludes the derivation of the steady, nonlinear weak form. To implement in the Firedrake library, we are required to add the three equations together in order to solve the implicit system of equations together. The following equation is used in the Firedrake library [10]:

Steady, Nonlinear Model Weak Form

$$\sum_{K\epsilon T}\iint_K \Big[\beta\sigma_x p - G_{winds}p + rqp + \nu\nabla p\cdot\nabla q - \nabla p\cdot(\hat{k}\times\vec{\sigma})q + q\phi+\nabla\phi\cdot\vec{\sigma}+\frac{1}{Bu}\psi\phi+\vec{v}\cdot\vec{\sigma}+\psi\nabla\cdot\vec{v}\Big]\, dA = 0. \tag{3.15}$$

Steady Linear Model

The derivation of the steady, linear model follows. When we neglect the nonlinear terms of equation 3.15, we obtain the following:

Steady, Linear Model Weak Form

$$\sum_{K\epsilon T}\iint_K \Big[\beta\sigma_x p - G_{winds}p + rqp + \nu\nabla p\cdot\nabla q + q\phi + \nabla\phi\cdot\vec{\sigma} + \frac{1}{Bu}\psi\phi + \vec{v}\cdot\vec{\sigma} + \psi\nabla\cdot\vec{v}\Big]\, dA = 0. \tag{3.16}$$

The steady linear model has been used in this work to analyze how the steady wind-driven gyre solutions depend on the bottom drag coefficient, beta parameter, and the Burger number.

3.2 Time Dependent Model

The derivation of the weak form for the time dependent nonlinear QG problem follows the same procedure as was saw in the steady problem. Below is the resulting weak form for the vorticity equation:

$$\sum_{K\epsilon T}\iint_K \Big[p\partial_t q + \beta\sigma_x p - G_{winds}p + rqp + \nu\nabla p\cdot\nabla q - \nabla p\cdot(\hat{k}\times\vec{\sigma})q\Big]\, dA = 0. \tag{3.17}$$

Note this is identical to equation 3.12 except for the presence of the time dependent term on the left hand side. To manage the time dependency, Backward Euler is applied, which says for [12] $dy/dt = f(t,y)$,

$$y^{n+1} = y^n + \Delta t\ f(t^{n+1}, y^{n+1}). \tag{3.18}$$

This method is unconditionally stable and first order accurate, which means that the local discretization error is $\mathcal{O}(h)$ [12]. After applying Backwards Euler to equation 3.17 produces:

$$\sum_{K\epsilon T}\iint_K pq^{n+1}\, dA = \sum_{K\epsilon T}\iint_K pq^n - \Delta t\Big[\beta\sigma_x^{n+1}p - G_{winds}p + rpq^{n+1} + \nu\nabla p\cdot\nabla q^{n+1} - \nabla p\cdot(\hat{k}\times\vec{\sigma}^{n+1})q^{n+1}\Big]\, dA. \tag{3.19}$$

Similar to the steady model, in order to implement in the Firedrake library we add the three weak forms but this time we use equation 3.19 instead of equation 3.12. That is, we add equations 3.19, 3.13 and 3.14 to obtain:

Time-Dependent, Nonlinear Weak Form

$$\sum_{K\epsilon T}\iint_K pq^{n+1}\,dA = \sum_{K\epsilon T}\iint_K \Bigg(pq^n - \Delta t\Big[\beta\sigma_x^{n+1}p - G_{winds}p + rpq^{n+1} + \nu\nabla p\cdot\nabla q^{n+1} - \nabla p\cdot(\hat{k}\times\vec{\sigma}^{n+1})q^{n+1}\Big] + \nabla\phi\cdot\vec{\sigma} + \frac{1}{Bu}\phi\psi + \phi q\vec{v}\cdot\vec{\sigma} + \psi\nabla\cdot\vec{v}\Bigg)\,dA. \tag{3.20}$$

Linear Case

The weak form for the time-dependent, one layer, linear model with a Backwards Euler is shown below.

Time-Dependent, Linear Model with Backwards Euler Weak Form

$$\sum_{K\epsilon T}\iint_K pq^{n+1}\,dA = \sum_{K\epsilon T}\iint_K \Bigg(pq^n - \Delta t\Big[\beta\sigma_x^{n+1}p - G_{winds}p + rpq^{n+1} + \nu\nabla p\cdot\nabla q^{n+1}\Big] + \nabla\phi\cdot\vec{\sigma} + \frac{1}{Bu}\phi\psi + \phi q\vec{v}\cdot\vec{\sigma} + \psi\nabla\cdot\vec{v}\Bigg)\,dA, \tag{3.21}$$

3.3 Linear Stability Model

The linear stability model derived in Section 2.3, as well as the associated potential vorticity and velocity equations as stated in equations 3.1 and 3.2 can be written as follows after

dropping the primes for convenience:

$$\begin{aligned}\partial_t q + \beta\sigma_x + [(\hat{k}\times\vec{S})\cdot\nabla]q + [(\hat{k}\times\vec{\sigma})\cdot\nabla]Q &= -rq + \nu\nabla^2 q,\\ q &= \nabla^2\psi - \frac{1}{Bu}\psi,\\ \vec{\sigma} &= \nabla\psi.\end{aligned}$$

As done previously, we multiply each equation by an associated test function, ϕ, p and v respectively then integrate over the domain. We apply integration by parts and the divergence theorem, then collect boundary terms on the right hand side:

$$\begin{aligned}\sum_{K\epsilon T}\iint_K \Big[p\partial_t q + \beta\sigma_x p - \nabla p\cdot(\hat{k}\times\vec{S})q - \nabla p\cdot(\hat{k}\times\vec{\sigma})Q + rqp + \nu\nabla p\cdot\nabla q\Big]\,dA =\\ \sum_{K\epsilon T}\oint_{\partial K}\Big[-pq(\hat{k}\times\vec{S})\cdot\hat{n} - pQ(\hat{k}\times\vec{\sigma})\cdot\hat{n} + \nu p\nabla q\cdot\hat{n}\Big]\,ds,\end{aligned} \tag{3.22}$$

$$\sum_{K\epsilon T}\iint_K \Big[q\phi + \nabla\phi\cdot\vec{\sigma} + \frac{1}{Bu}\psi\phi\Big]dA = \sum_{K\epsilon T}\oint_{\partial K}\phi\vec{\sigma}\cdot\hat{n}\,ds, \tag{3.23}$$

$$\sum_{K\epsilon T}\iint_K \Big[\vec{\sigma}\cdot\vec{v} + \psi\nabla\cdot\vec{v}\Big]\,dA = \sum_{K\epsilon T}\oint_{\partial K}\psi\vec{v}\cdot\hat{n}\,ds. \tag{3.24}$$

Next, we apply boundary conditions as described in section 2.2.4 and apply a backwards Euler time stepping scheme to the governing equation. The total weak form becomes:

$$\begin{aligned}\sum_{K\epsilon T}\iint_K pq^{n+1}\,dA = \sum_{K\epsilon T}\iint_K \Big(pq^n + \Delta t\big[-\beta p\sigma_x^{n+1} + \nabla p\cdot(\hat{k}\times\vec{S})q^{n+1}\\ +\nabla p\cdot(\hat{k}\times\vec{\sigma}^{n+1})Q - rpq^{n+1} - \nu\nabla p\cdot\nabla q^{n+1}\big]\Big)\,dA,\end{aligned} \tag{3.25}$$

$$\sum_{K\epsilon T}\iint_K \Big[q\phi + \nabla\phi\cdot\vec{\sigma} + \frac{1}{Bu}\psi\phi\Big]dA = 0, \tag{3.26}$$

$$\sum_{K\epsilon T}\iint_K \Big[\vec{\sigma}\cdot\vec{v} + \psi\nabla\cdot\vec{v}\Big]\,dA = 0. \tag{3.27}$$

As previously, we add the three equations together in order to solve the implicit system

of equations together in the Firedrake library. The total weak form for the system becomes:

Time Linear Stability Model with Backward Euler Weak Form

$$\begin{aligned}\sum_{K\epsilon T}\iint_K pq^{n+1}\,dA = \sum_{K\epsilon T}\iint_K \Bigg(pq^n - \Delta t\Big[\beta p\sigma_x^{n+1} - \nabla p\cdot(\hat{k}\times\vec{S})q^{n+1} \\ -\nabla p\cdot(\hat{k}\times\vec{\sigma}^{n+1})Q + rpq^{n+1} + \nu\nabla p\cdot\nabla q^{n+1}\Big] \\ +q\phi + \nabla\phi\cdot\vec{\sigma} + \frac{1}{Bu}\psi\phi + \vec{\sigma}\cdot\vec{v} + \psi\nabla\cdot\vec{v}\Bigg)\,dA.\end{aligned} \tag{3.28}$$

In linear stability theory it is expected that the steady solution be an exact solution to the nonlinear governing equations. In our work we are finding numerical solutions and therefore exact solutions are not possible. Also, we focus on a solution to the linear problem since this is simpler in terms of computations. Initially, we investigated and obtained nonlinear solutions, however for the weak winds that are considered in this thesis, there was very little difference between the two. This is why we focus on linear solutions instead. However, it should be recognized that an improvement to this work should be to analyze the stability of a solution to the nonlinear steady equations.

In the next chapter, we present the solutions obtained by implementing the weak forms derived here.

Chapter 4

Results

In this chapter we present results from two different physical regimes. The first regime is the classical wind-driven gyre, which applies the parameters used by [30] and [17] for the purpose of comparing and validating. The second regime uses parameters associated with the Beaufort gyre, and investigates the effects of both the beta parameter and the Burger number. For each regime, we present three different solutions: steady solutions to the wind-driven gyre problem (equation 2.48), time-dependent solutions to the full nonlinear problem (equation 2.44) and time-dependent solutions to the linear stability problem (equation 2.68). The methods that were used to solve the models have been discussed in Chapter 3.

4.1 The Classical Wind-Driven Gyre

4.1.1 Parameters

Prior to investigating the dynamics of the Beaufort gyre, we sought to validate our model by comparing to work previously done by [30] and [17]. These two references investigate the effects of viscosity on both the Munk model and a rotating SW model in dimensional form. They found the boundary layer thicknesses associated with laminar flow, eddy fields and turbulent flow for a square domain of length 4000 km in both x and y directions. Although they considered several types of boundary layers, the work done in this thesis only used the results associated with the Munk boundary layer. [30] and [17] varied the viscosity coefficient in order to control the Munk layer thickness. In this thesis, we control the boundary

Western Boundary Thickness		
Boundary Thickness (%)	Flow Regime	Associated Bottom Drag
10	Laminar	0.01
5	Laminar	0.005
2.5	Laminar	0.0025
1.25	Laminar	0.00125
0.625	Eddies	0.000625
0.3125	Turbulent	0.0003125

Table 4.1: The boundary layer thicknesses with the associated flow regimes determined by [30][17], and the necessary bottom drag coefficients in order to obtain the given thicknesses. This has been implemented for the classical wind-driven gyre problem.

layer thickness as well, but instead we used a Stommel layer which requires varying the bottom drag coefficient. To be specific, we wanted the same boundary thicknesses as [30] and [17] in order to obtain similar flow regimes. However, the work done in this thesis is non-dimensional, which translates to a unit square. Due to the difference in domain sizes, the boundary thickness was measured as a percentage of the whole domain. When calculating the boundary layer thickness, we choose a small beta value 0.1 for simplicity. In Table 4.1, we list the bottom drag coefficients needed to produce the same boundary layer thicknesses used by [30] and [17], as well as the flow regimes we expect to reproduce. The work done in this thesis tested each case listed, but the western boundary of 0.625% is of particular interest as it is expected to lead to eddies. Based on the results obtained from [30] and [17], we should expect to see indications of instabilities by day 50, unfortunately this was not observed. Using Table 2.1, we may obtain the non-dimensional equivalent to fifty days by multiplying by a factor of U/L. For simplicity, we used the length and velocity scale associated with the eddies regime obtained by [30] and [17]: 12500 m and 0.7 ms^{-1} respectively. The resulting non-dimensional time we should expect to see indications of eddies is $\hat{t} = 242$. In implementation, we will take time steps equivalent of one day, $d\hat{t} = 5$.

The remaining parameters needed to implement the Stommel-Munk Model are listed in Table 4.2. Similar to the beta parameter, the inverse Burger number was also taken to be small for simplicity. The scales used for length, depth, density and wind stress were taken to be the same as presented in [30] and [17]. As mentioned in Section 2.2, the wind forcing term, G_{winds}, forces the vorticity and is defined by:

$$G_{winds} = \mathbf{k} \cdot \nabla \times \tau, \tag{4.1}$$

Classical Regime: Implemented Parameters		
Scales		
Length	L	12500m
Velocity	U_{WBC}	$7 \times 10^{-1}\text{ms}^{-1}$
Depth	H	500 m
Density	ρ_0	1000 $kg\ m^{-2}$
Wind Stress	τ_0	0.1 $N\ m^{-2}$
Non-dimensional Values		
Viscosity Coefficient	$\hat{\nu}$	0.001
Bottom Drag Coefficient	$\hat{r}$	0.01 to 3.125×10^{-4}
Beta Parameter	$\hat{\beta}$	0.1
Inverse Burger Number	F	0.1
Wind Forcing	$\hat{G}_{winds}$	$-\frac{L}{U^2}\frac{\tau_0 \pi}{\rho_0 H}\sin(\pi \hat{y})$

Table 4.2: The values used during implementation of the models discussed in Section 2.44 and 2.3 under the classical regime. The exact values of bottom drag may be found in Table 4.1.

where [30] and [17] define the dimensional wind stress by:

$$\tau = -\frac{\tau_0}{\rho_0 H}\cos(\frac{\pi y}{L}). \tag{4.2}$$

This is used as it is known to produce a single gyre. We again use Table 2.2.3 to obtain the non-dimensional form and multiply G_{winds} by a factor of L^2/U^2. In Figure 4.1we present the curl of the wind over the domain, which contributes zero vorticity at the northern and southern boundaries, and contributes negative vorticity in the mid-meridional area.

The mesh used in this section was 400 in the x direction and 400 in the y direction. The solutions obtained in this section used the University of Waterloo's Math faculty remote machine, cpu141. Early computations were run in parallel, however many of the plots presented were obtained in serial computing. Due to numerical divergence issues the classical winds were reduced by a factor of 10^{-8} during implementation. This seems to be due to difficulties with the linear solvers converging and even though we have tried different solvers and different time steps, we were not able to solve the equations in the regions that gives rise to physical instabilities. Unfortunately these tests did not allow for solution convergence while using the full winds.

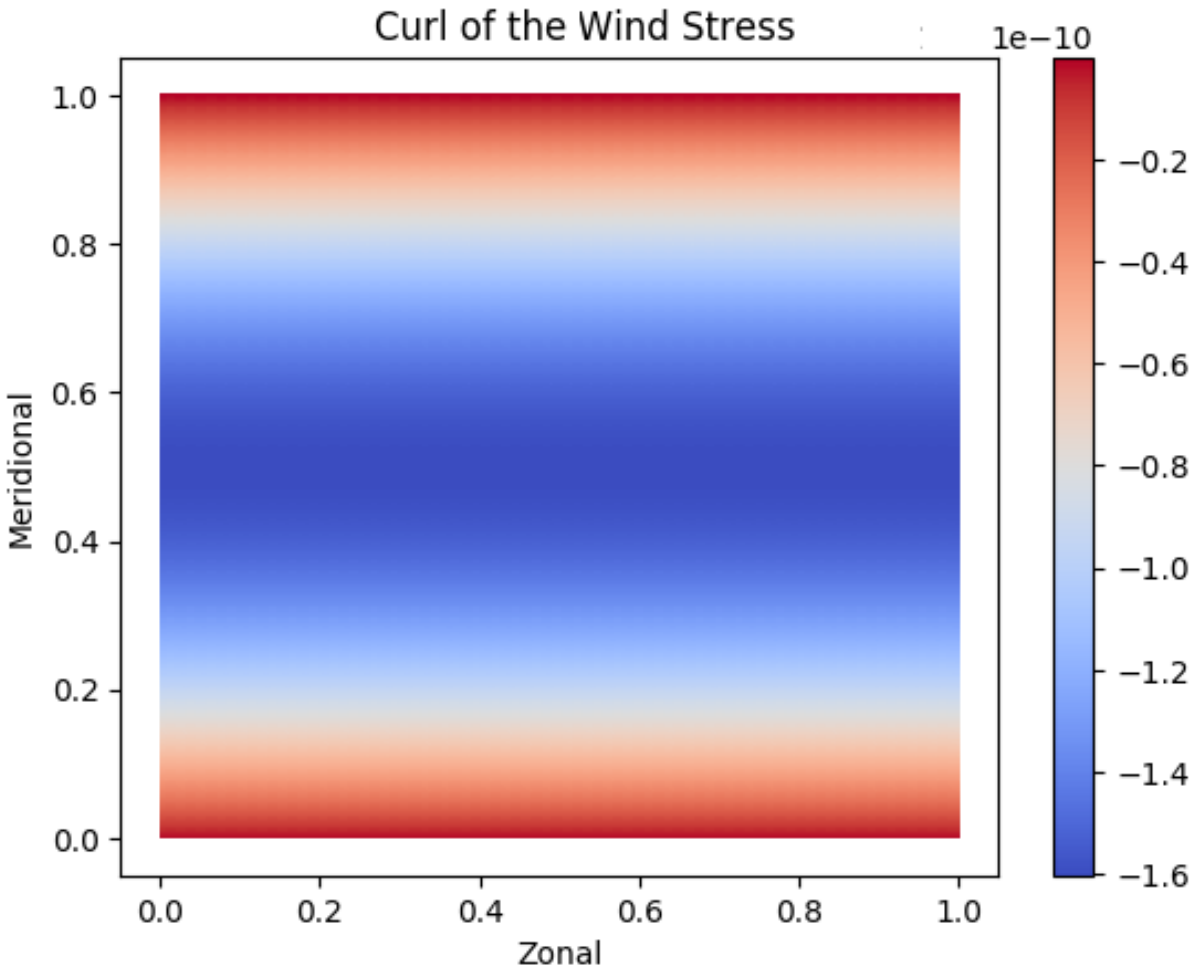

Figure 4.1: The curl of the wind stress which drives the gyre in the classical regime.

4.1.2 Linear Steady Solutions

We now present the solutions to the steady Stommel-Munk Model, equation 2.48, using the parameters listed in Table 4.1 and Table 4.2. In Figure 4.2 we show the streamfunction solution overlaid with the velocity where we have taken bottom drag to be $r = 0.005$, producing a western boundary thickness of 0.05, or 5%. The zonal direction represents west to east, along latitudinal lines, and the meridional direction represents south to north along longitudinal lines [19]. The velocity displays a clear anti-cyclonic (clockwise) direction, which is expected for the positive valued Coriolis parameter associated with the northern hemisphere. As the flow nears the western boundary, the velocity increases due to western intensification, which is a result of the Coriolis force. In Figure 4.3 and Figure 4.4, we present the steady streamfunction and potential vorticity solutions for several values of bottom drag. In order to see the details of the spatial structure, we use different colour bars in each plot. In Figure 4.3a, we again show the streamfunction for a western boundary thickness of 5% but this time without the quiver plot. The associated potential vorticity solution is presented in Figure 4.4a, which has been magnified in on the western boundary in order to show the results more clearly as we reduce the boundary. To be specific, we show 10% of the horizontal domain, along the western boundary. We obtain Figure 4.3b and Figure 4.4b by reducing the bottom drag by a factor of two, thus reducing the western boundary by a factor of two as well. This results in an increased northward velocity along the western boundary, as well as slightly increased values of potential vorticity closer to the western boundary. We continue to reduce the bottom drag and therefore the thickness of the western boundary current in the remaining sub-figures of both Figure 4.3 and 4.4. As we do so, the intensification of velocity and the potential vorticity continue to increase, becoming closer to the western boundary. Although the western boundary thickness in Figure 4.3d and Figure 4.4d is expected to produced eddies based on the work done by [30] and [17], we cannot see instabilities here, in the steady model. To observe the instabilities we must perturb the steady solutions and look at how the perturbations grow in time. These results are presented in Section 4.1.4.

4.1.3 Nonlinear Time-Dependent Solutions

Based on previous works, we expect the time dependent solutions to converge to the steady solutions as they have previously been found to be asymptotically stable. In Figure 4.5 we confirm this for a western boundary thickness of 0.05 or 5%. Due to numerical divergence issues, we were unable to show the case for a western boundary thickness of 0.625%. We initialize the simulation with zero potential vorticity. At $\hat{t} = 5$, Figure 4.5a, the

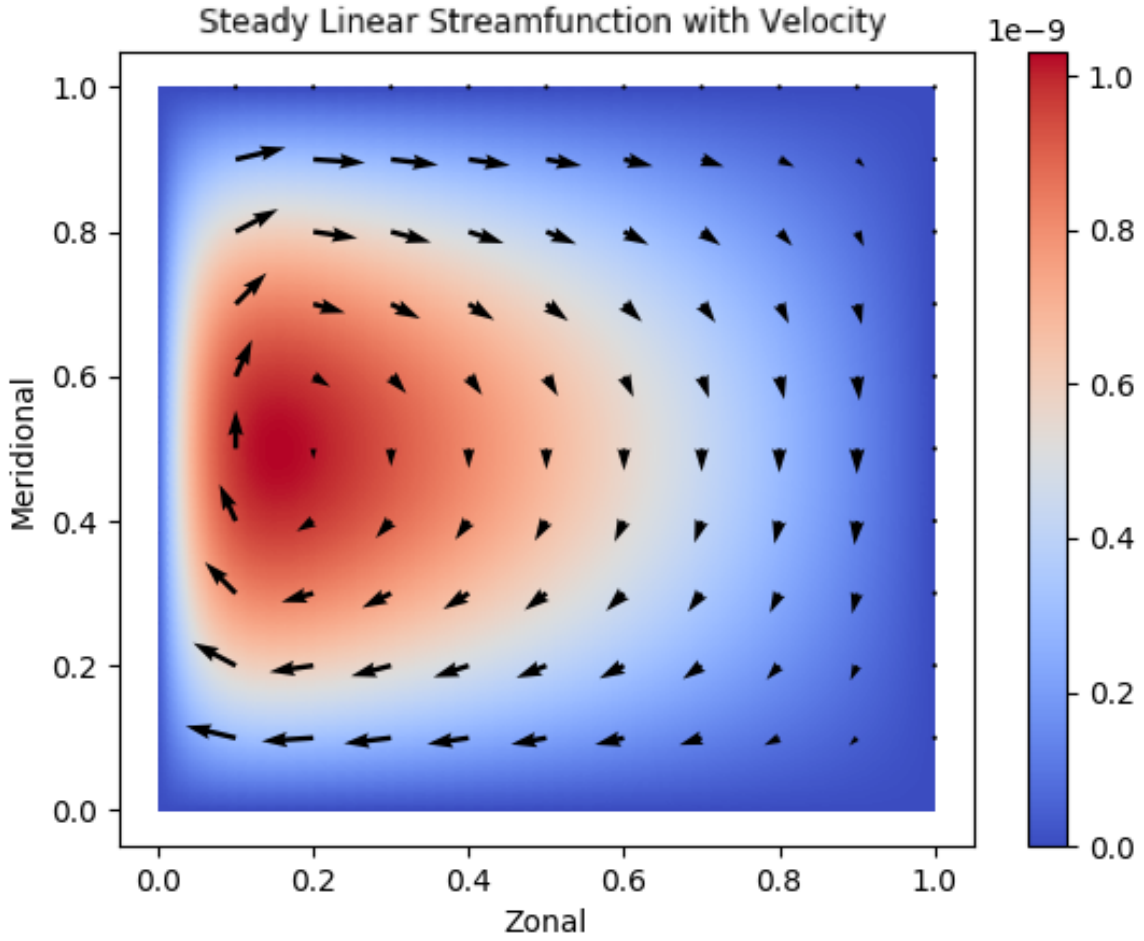

Figure 4.2: The steady linear streamfunction imposed with the associated velocity under the classical regime for equation 2.48. The bottom drag has been taken to be 0.05, producing a western boundary thickness of 5%.

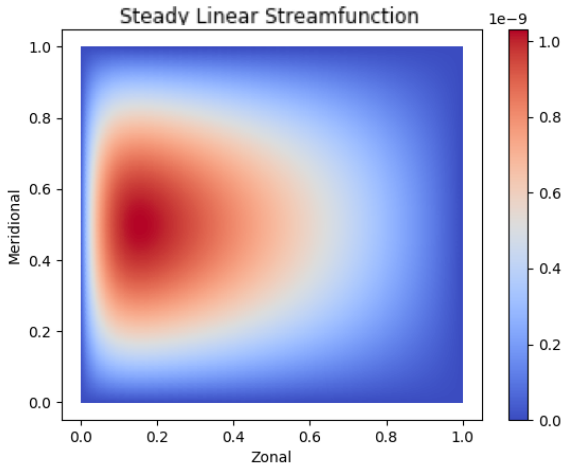

(a) Western boundary thickness of 5%.

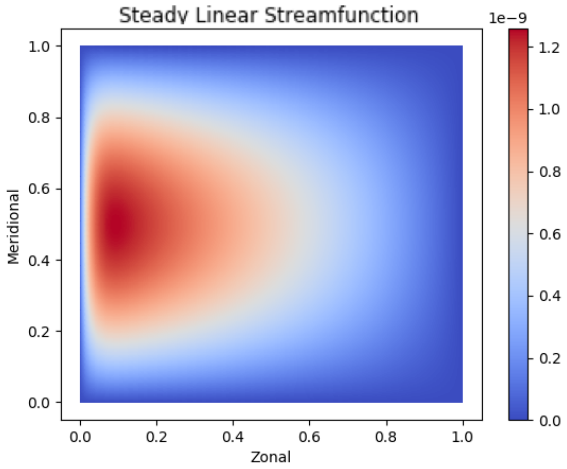

(b) Western boundary thickness of 2.5%.

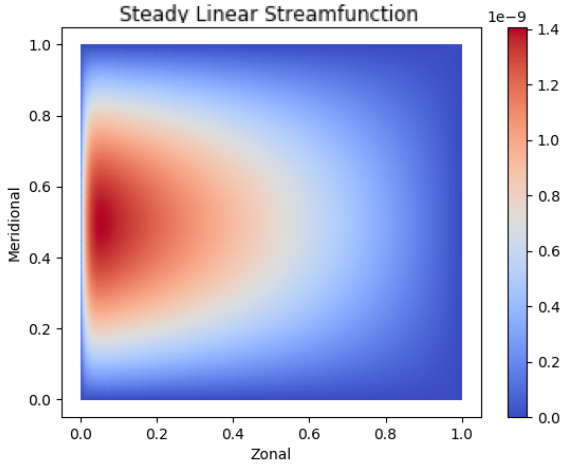

(c) Western boundary thickness of 1.25%.

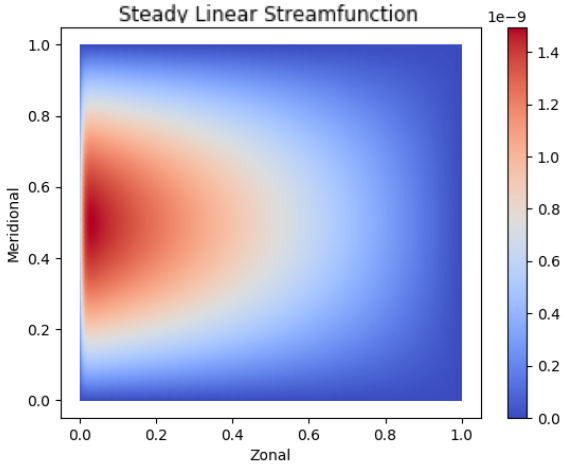

(d) Western boundary thickness of 0.625%.

Figure 4.3: The streamfunction solutions to the steady, linear model (2.48) under the classical regime with bottom drag of 0.005, 0.0025, 0.00125 and 0.000625 respectively. The associated western boundary thickness has been listed below each figure, and the associated potential vorticity solutions may be found in Figure 4.4. Due to the wide range of values, each figure has an individual color bar.

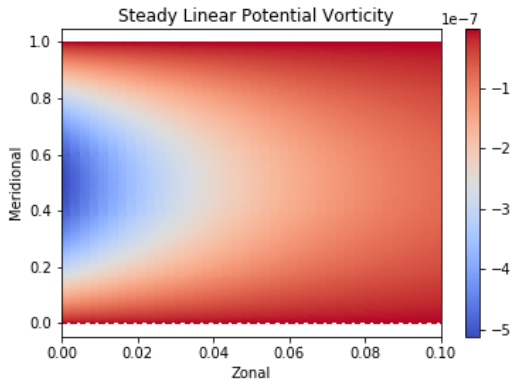

(a) Western boundary thickness of 5%.

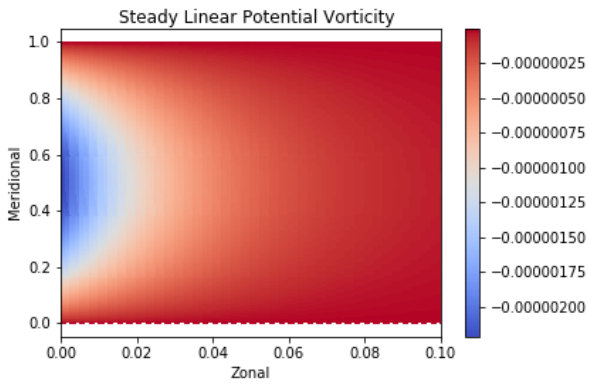

(b) Western boundary thickness of 2.5%.

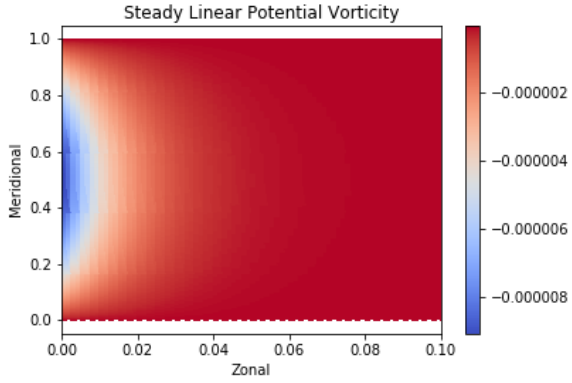

(c) Western boundary thickness of 1.25%.

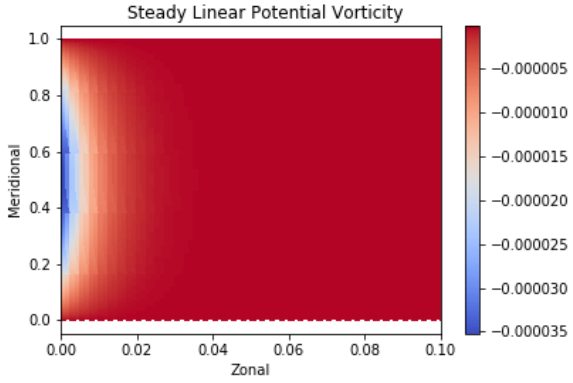

(d) Western boundary thickness of 0.625%.

Figure 4.4: The steady linear potential vorticity under the classical regime for equation 2.48, with bottom drag of 0.005, 0.0025, 0.00125 and 0.000625 respectively. The associated western boundary thickness has been listed below each figure, and the associated streamfunction solutions may be found in Figure 4.3. Note, these plots have been magnified in on the western boundary in order to show the spatial structure. Due to the wide range of values, each figure has an individual color bar.

streamfunction is symmetrical in both latitude and longitude. The associated potential vorticity, Figure 4.5b, is almost symmetrical, tending slightly to the left. We evolve the potential vorticity and by $\hat{t} = 105$ the solution has moved towards the western boundary, shown in Figures 4.5d. The associated streamfunction solution, Figures 4.5c begins to show western intensification. That is, the solution begins to favor the western boundary and velocities increase. By $\hat{t} = 205$, the potential vorticity has converged to the steady solution, shown in Figure 4.4a which has been measured by the norm of the error to an accuracy of two decimals. The solution has localized in the western boundary and has increased in magnitude. This confirms the nonlinear time dependent solutions provide reasonable results.

We may now use this nonlinear model to evolve perturbations on the steady wind-driven gyre solutions. We will solve for the steady potential vorticity solution, and add small randomized perturbations across the domain. We use this as the initial potential vorticity, and for numerical convergence purposes, we continue to show for a 5% western boundary thickness. The nonlinear perturbation evolution has been plotted in Figure 4.7, and the associated streamfunction has been plotted in Figure 4.6. At $\hat{t} = 5$, the perturbation remains randomized and does not show any specific spatial structure. By $\hat{t} = 155$ (Figure 4.7b) the perturbations begin to grow along the western boundary, and shrink in the rest of the domain. This structure intensifies as we continue to evolve the perturbation. The associated streamfunction displays westward propagation of basin modes, shown in Figure 4.6 [20] [35]. These results will be compared to the linear stability solutions. As discussed in Section 2.3, the linear stability solutions should be qualitatively comparable to the nonlinear perturbation solutions. We present the linear stability solutions in the following section.

4.1.4 Linear Stability Solutions

We now present the solutions to the linear stability model, equation 2.68. In Figure 4.8, we present the evolution of the streamfunction perturbations for a western boundary thickness of 0.05 or equivalently 5%. In the few time steps we share, there is a basin mode propagating towards the western boundary. These modes continue to form and propagate westwards for the duration of the simulation. In Figure 4.9, we present the associated potential vorticity solutions. The spatial structure is very similar to the nonlinear perturbation evolution solutions in Figure 4.6, with greatest perturbation growth along the western boundary. When compared to the streamfunction perturbations and potential vorticity perturbations (Figures 4.6 and 4.7) from the nonlinear, time-dependent, we note the magnitudes are larger here, which may indicate weaker dissipation in the stability model. Based on the

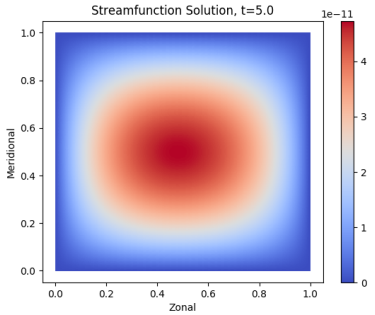

(a) $\hat{t} = 5.0$

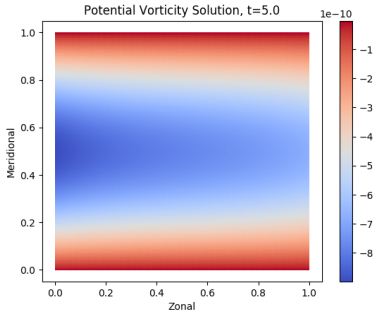

(b) $\hat{t} = 5.0$

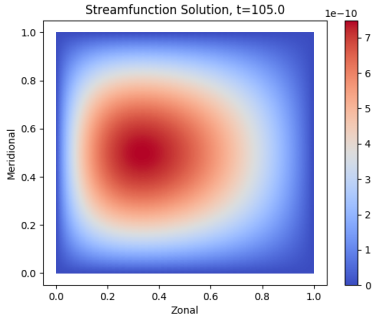

(c) $\hat{t} = 105.0$

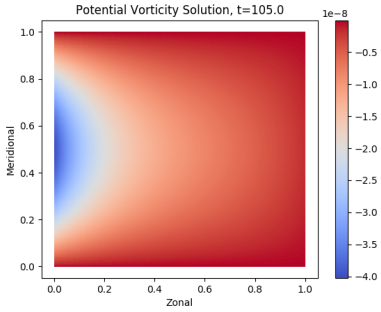

(d) $\hat{t} = 105.0$

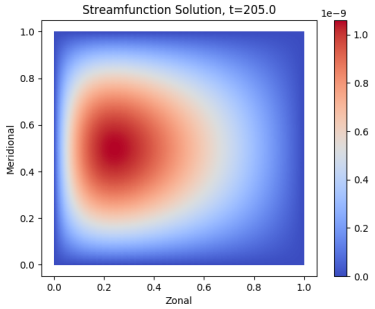

(e) $\hat{t} = 205.0$

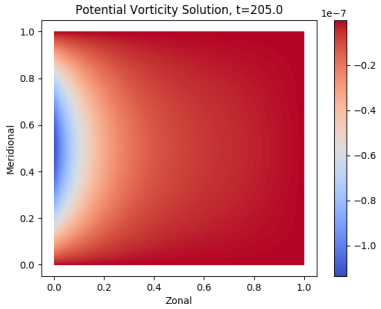

(f) $\hat{t} = 205.0$

Figure 4.5: The streamfunction (left) and the potential vorticity (right) to the nonlinear, time dependent model (2.44) under the classical regime for bottom drag 0.005 with an associated western boundary thickness of 5%. These solutions have been initialized with zero potential vorticity and evolved until they converged to the steady solution as seen in Figure 4.3a. Due to the wide range of values, each figure has an individual color bar.

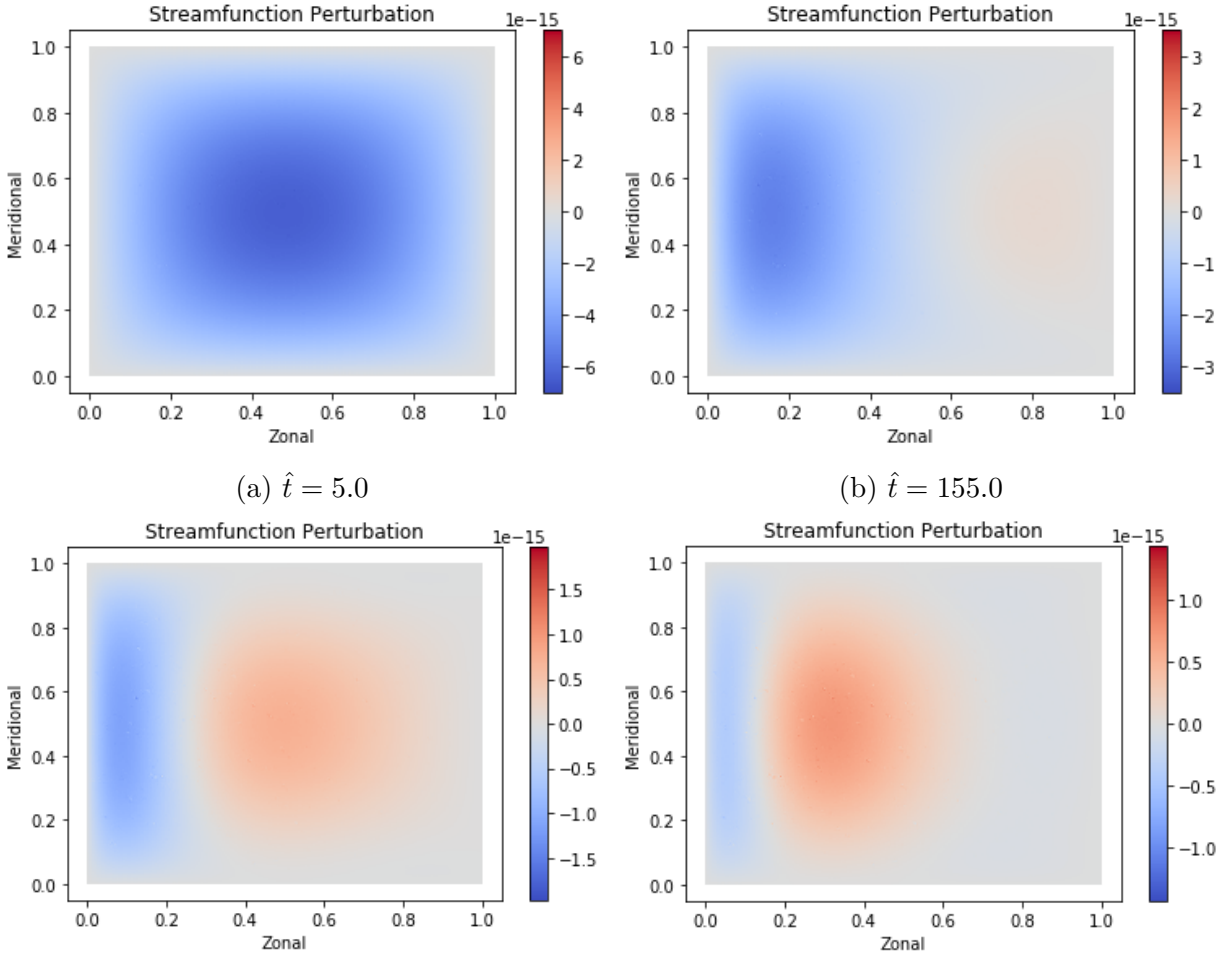

(a) $\hat{t} = 5.0$

(b) $\hat{t} = 155.0$

(c) $\hat{t} = 255.0$

(d) $\hat{t} = 355.0$

Figure 4.6: The streamfunction in the nonlinear, time dependent model (2.44) under the classical regime for bottom drag 0.005 with an associated western boundary thickness of 5%. These solutions have been initialized with a perturbed basic state. The associated potential vorticity is seen in Figure 4.7

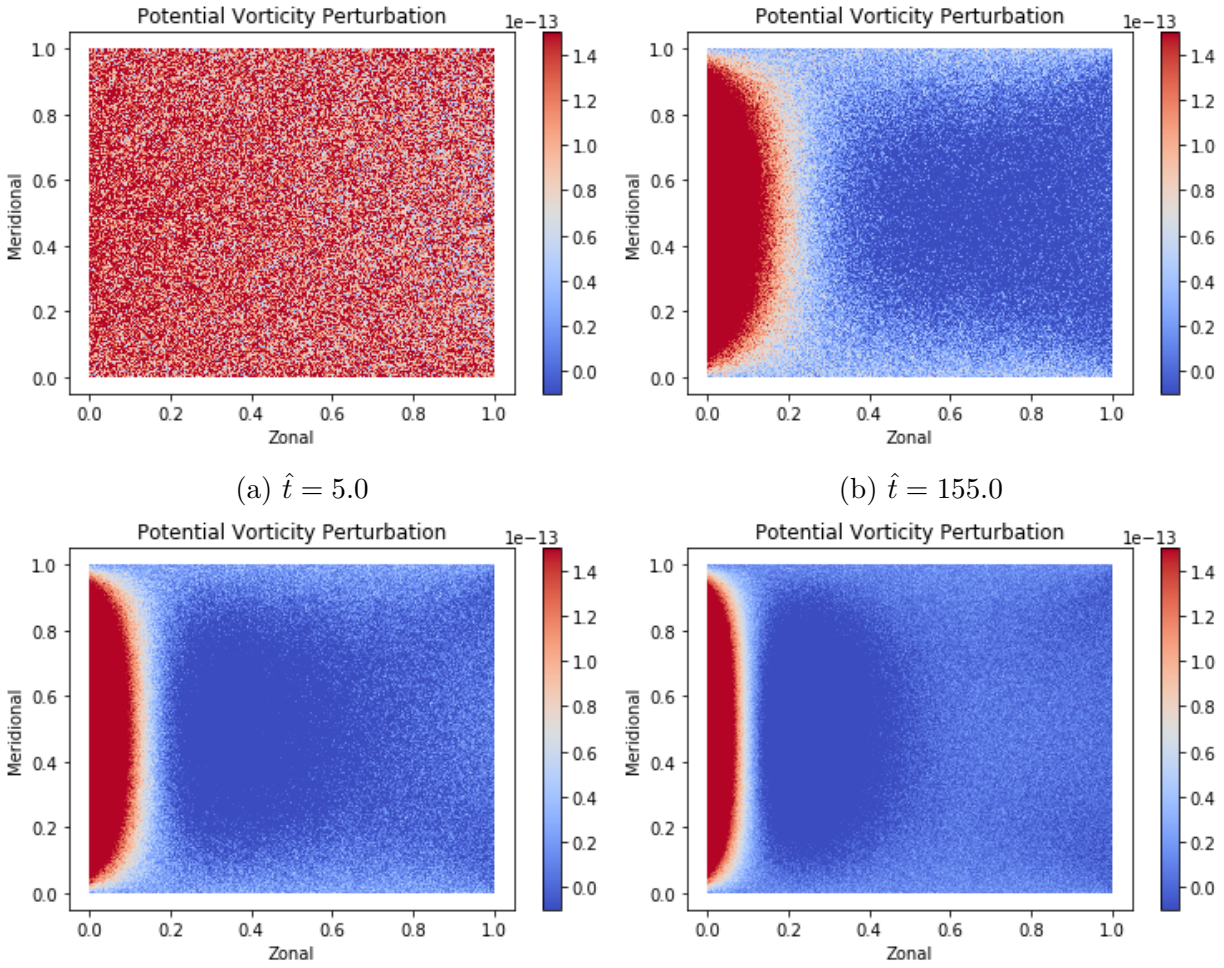

(a) $\hat{t} = 5.0$

(b) $\hat{t} = 155.0$

(c) $\hat{t} = 255.0$

(d) $\hat{t} = 355.0$

Figure 4.7: The potential vorticity in the nonlinear, time dependent model (2.44) under the classical regime for bottom drag 0.005 with an associated western boundary thickness of 5%. These solutions have been initialized with a perturbed basic state. The associated streamfunction is seen in Figure 4.6.

findings of [30] and [30], we expect to see instabilities arise for a western boundary of the given thickness. We discuss in the final chapter why we may not see instabilities.

4.2 The Beaufort Gyre

4.2.1 Parameters

In this section the parameters we have chosen for the QG model to represent the idealized Beaufort gyre are presented. Being in the Arctic, the study area experiences seasonal changes and varies significantly throughout the year [33]. For this reason, the parameters listed may be presented as a range, and have been obtained from various observational and technical papers, as well as calculated as shown here.

Physical Parameters		
Parameter	Variable	BG Value
Latitude	θ	75^o to 85^o [15][43]
Longitudinal	ϕ	130^o to 170^o [15]
Diameter	L	500 km to 1500 km [15][38]
Shear Length Scale	L_{sh}	50 km [22]
Top mean thickness	H_1	150 m [22]
Bottom mean thickness	H_2	700 m [22]
Halocline layer thickness	H_a	50 m[22]
Top Layer Density	ρ_1	1023 kg m^{-2} [22][23]
Bottom Layer Density	ρ_2	1027 kg m^{-2} [26]

Table 4.3: Physical parameters associated with the Beaufort gyre.

In Table 4.3, we include the physical measurements associated with the Beaufort gyre. The study area is circular in shape and ranges from a latitude of 75^o to 85^o, and the longitudinal range is between 130^o and 170^o [15] [43]. This provides a maximal diameter between 800 km and 1500 km, which is consistent with other idealized models, such as [22], [36], or [6]. However, as mentioned previously, the Beaufort gyre changes drastically from season to season, and has been recorded to range between 500 km to 800 km in diameter [33][38]. For the done here to model the Beaufort gyre, we will use a circle domain with diameter 800 km and use a length scale associated with the dominant flow, approximately one fifth of the domain or 160 km. Due to the fresh upper layer and the salty lower layer,

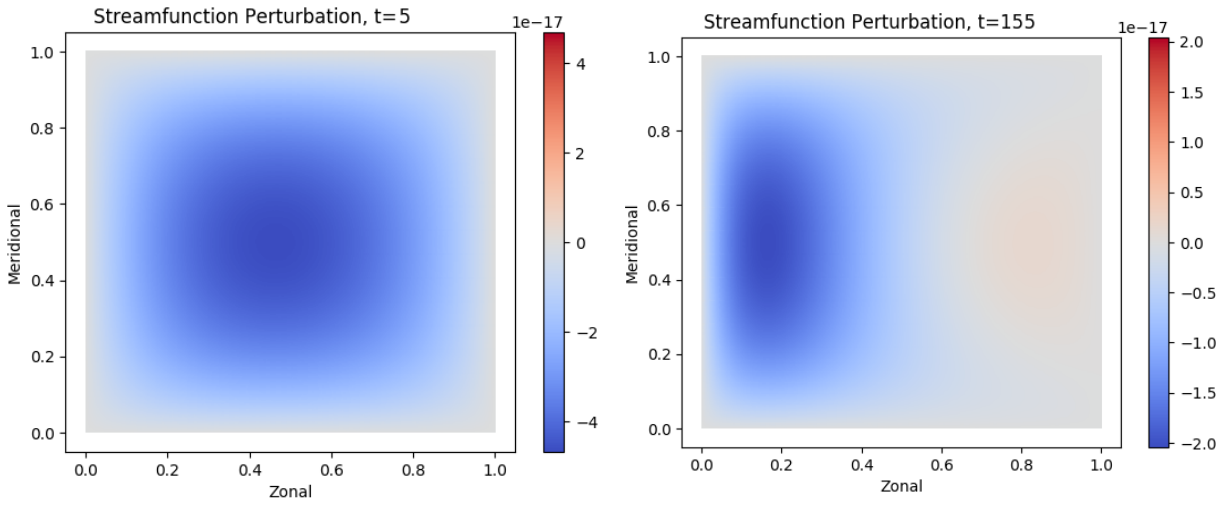

(a) $\hat{t} = 5$

(b) $\hat{t} = 155$

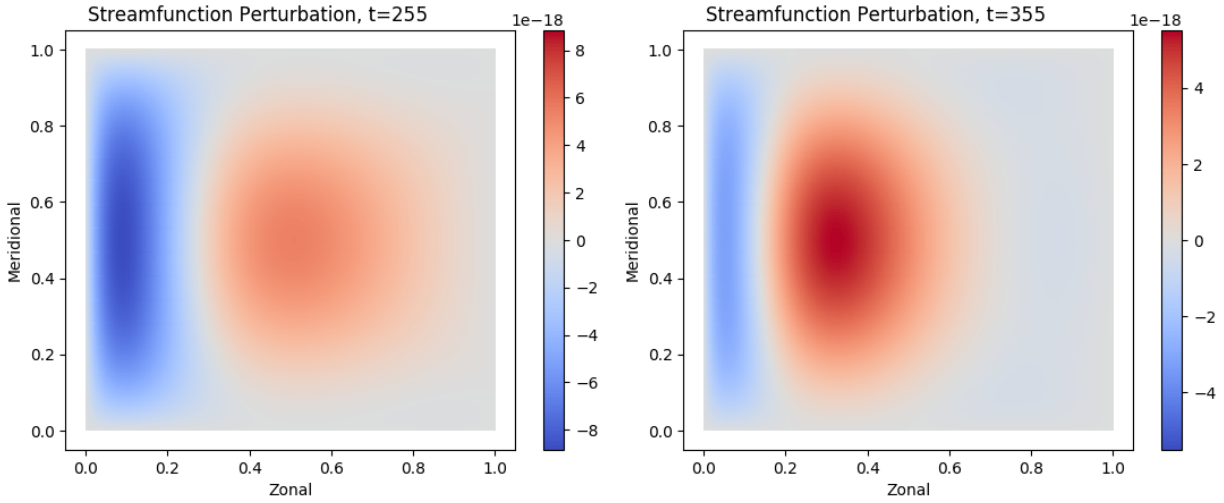

(c) $\hat{t} = 255$

(d) $\hat{t} = 355$

Figure 4.8: The streamfunction in the linear stability model (2.68) under the classical regime for bottom drag 0.005 with an associated western boundary thickness of 5%. These solutions have been initialized with a perturbation for potential vorticity. The associated potential vorticity is seen in Figure 4.9.

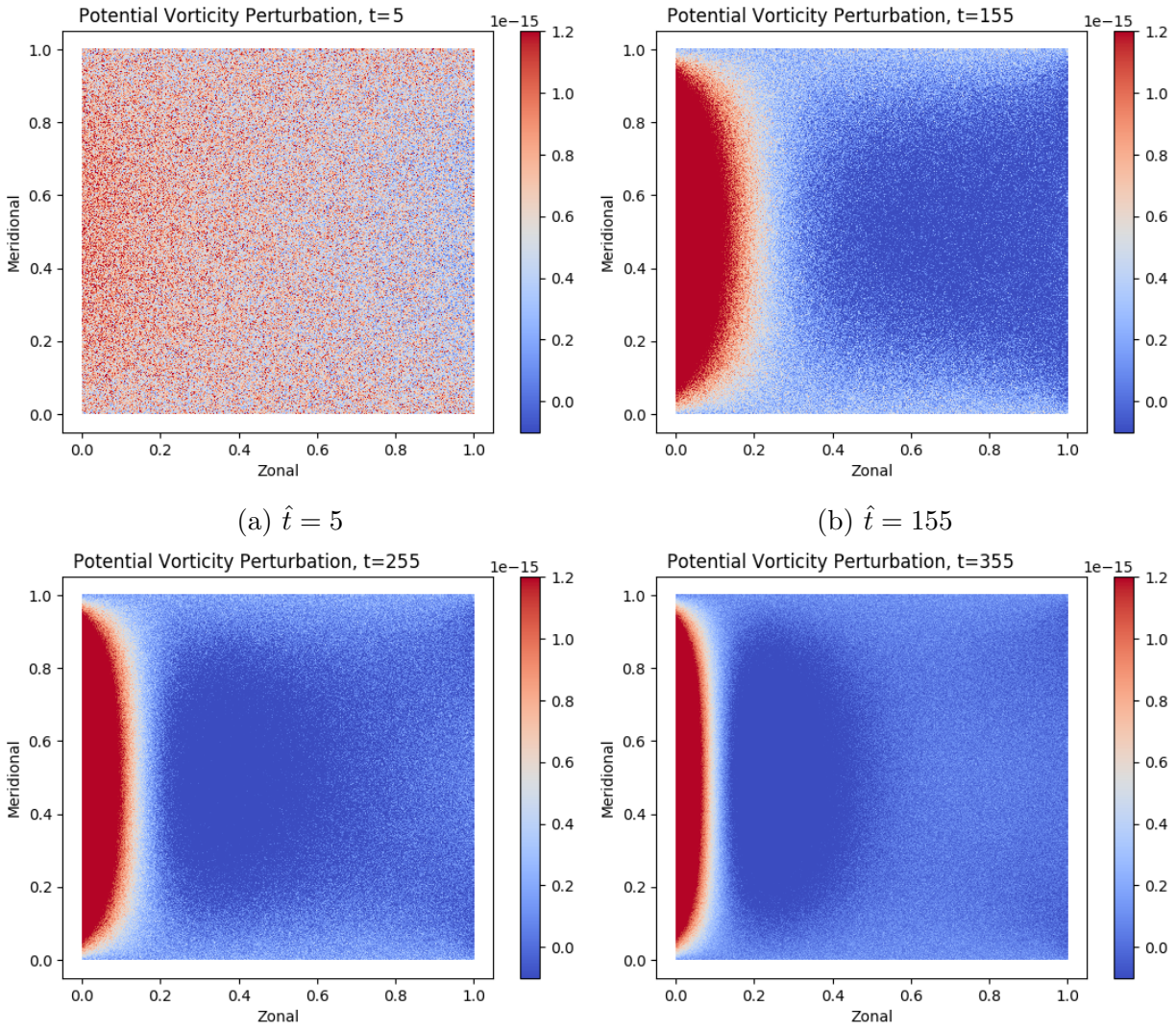

(a) $\hat{t} = 5$

(b) $\hat{t} = 155$

(c) $\hat{t} = 255$

(d) $\hat{t} = 355$

Figure 4.9: The potential vorticity in the linear stability model (2.68) under the classical regime for bottom drag 0.005 with an associated western boundary thickness of 5%. These solutions have been initialized with a perturbation for potential vorticity. The associated streamfunction is seen in Figure 4.8.

the isopycnal has a region which rapidly changes and we may alternatively use the shear length scale, 50 km [22]. The circular domain is the first step in modelling the Beaufort gyre and common among idealized Beaufort gyre models, such as [43] [21]. Future work may look to involve a more precise coastline associated with the Beaufort gyre. In regards to the vertical, idealized models used in other studies treat the fresh water and salt water content as two distinct layers, with a transitional zone between called the halocline [22]. For the work done here, we focus on the layer most affected by the wind forcing; the top layer. However future work may incorporate the two layer model to better understand the vertical structure, such as the work done by [29] and [43]. In which case the measurements of the bottom layer become useful [15]. In Table 4.3, we also include the density and depth for both the active (top) layer and the bottom (passive) layer, which has been labelled by a subscript of 1 and 2 respectively.

In Table 4.4, we include the dimensional parameters that are more challenging to measure and have therefore been chosen based of several technical other papers. We choose to neglect the lateral viscosity for the Beaufort gyre regime because the dominant motion is in the centre of the domain away from the boundary and is assumed to have negligible effects on the solution. By taking viscosity to be zero, the governing model given by equation 2.44 is similar to the Stommel model. However we do not expect much western intensification because not much is observed, and we expect a weak beta effect based on the relative smallness of the domain, compared to the previous problem. In regards to the bottom drag, there is uncertainty around how to choose an exact value, however many papers have used an amplitude of $\mathcal{O}(10^{-3})$ such as [36][43][22][6]. Similarly, the common choice for idealized wind stress has varied and ranges between 0.015 Nm^{-2} and 0.02 Nm^{-2} [36][22][23]. For example, Davis et al. [6] varied wind forcing between 0.02 Nm^{-2} and 0.028 Nm^{-2}, and Manucharyan et al. [23] varied winds between 0.005 Nm^{-2} and 0.075 Nm^{-2}. Based on a mean stress of 0.064 Nm^{-2}, Martin et al. [24] showed that the Arctic ocean has experienced an increase in mean ocean stress between the years of 2000 and 2012 of approximately 9% per decade. While this provides evidence of a changing wind regime, the work done here used a constant magnitude for wind stress of 0.015 N m^{-2} unless otherwise indicated.

In Section 1.2 we introduced these parameters and provided brief discussions on their significance. The Coriolis parameter and the beta parameter have been calculated using the maximum latitude, $\theta = 85^o$, Earth's angular velocity, $\Omega = 7.27 \times 10^{-5}$ rads^{-1} and Earth's radius $a = 6.4 \times 10^6$m [9][3]. Note, we could alternatively use a quadratic Coriolis parameter, however as a first step we use a constant parameter on a beta plane. The Rossby radius of deformation has been calculated using values from Table 4.3, where the reduced gravity is defined by $g' = g\frac{\rho_2 - \rho_1}{\rho_2}$, ρ_1 is the top layer density, ρ_2 is the bottom

Varying Parameters		
Measure	Variable	BG Value
Viscosity	ν	0.0 m^2s^{-1}
Bottom Drag	r	0.002 s^{-1} [43][22]
Wind Stress	τ	0.015 N m^{-2} [36][22][23]

Table 4.4: Parameters associated with the Beaufort gyre that are more difficult to measure and therefore may vary between studies.

layer density and gravity is taken to be $g = 9.8$ m s^{-2}. Lastly, the Burger number has been calculated by using the calculated Rossby radius of deformation and a length scale of 160 km. The Coriolis parameter and the Rossby radius of deformation are consistent with other technical papers such as [22][40][36][22]. The beta parameter and the Burger number presented in this table are the exact values values associated with the Beaufort gyre. However, prior to implementing the exact Beaufort gyre parameters, we investigated the effects of the beta parameter and the inverse Burger number on the model solutions. In this thesis, we include the steady solutions associated for an inverse Burger number 10^{-3} and non-dimensional beta values 0, 1.024 and 10 to investigate the effects of the beta parameter. The second choice of beta is the non-dimensional value associated with the Beaufort gyre. As well, we include steady solutions for a beta and an inverse Burger number 0.1, 10.0 and 100.0. The results presented were chosen to show the overall effects. In Table 4.5 we show the parameters used in our calculations.

Thus far, this section has presented dimensional values for the necessary parameters associated with the Beaufort gyre. We now present Table 4.6, which includes the scales and non-dimensional values that were implemented in the governing models. The non-dimensional values were calculated using Table 2.1. Note, the wind forcing, plotted in Figure 4.10 has been taken to be the shape of a Gaussian function in order to obtain maximum wind forcing at the centre and zero wind forcing on the boundaries. The non-dimensional wind forcing was obtained by multiplying by a factor of L^2/U^2, where we take the length scale to be 160 km as previously and the typical velocity scale to be $0.05ms^{-1}$. The associated dimensional wind forcing is

$$G_{winds} = \frac{\tau_0}{\rho_0 L} \exp\left(\frac{-\hat{r}^2}{L^2}\right),$$

where r is the radial variable in polar coordinates. Note that L determines the natural decay scale of the gyre.

The solutions obtained in this section used the University of Waterloo's Math faculty

Calculated Parameters		
Term	Equation	BG Value
Coriolis Parameter	$f_o = 2\Omega \sin\theta$	1.4×10^{-4} s^{-1} [22][40][36][22]
Beta Parameter	$\beta = \frac{2\Omega}{a} \cos\theta$	2.0×10^{-12} s^{-1}m^{-1}
Reduced Gravity	$g' = g\frac{\rho_2 - \rho_1}{\rho_2}$	0.038 ms^{-1}
Rossby Radius of Deformation	$L_d = \frac{\sqrt{g'H}}{f_o}$	20 km [6] [36] [22][23]
Burger Number	$Bu = \frac{L_d^2}{L^2}$	0.016

Table 4.5: The calculated parameters for the Beaufort gyre using the values from the Table 4.3. We have introduced Ω and a, which are the Earth's angular velocity, the Earth's radius and the buoyancy frequency respectively.

Beaufort Gyre Regime: Implemented Parameters		
Scales		
Length	L	1.6×10^5 m
Velocity	U	$0.03 - 0.05$ m s^{-1} [16] [26][1]
Depth	H	200 m
Density	ρ_0	1025 kg m^{-2}
Wind Stress	τ_0	0.015 N m^{-2}
Non-dimensional Values		
Bottom Drag Coefficient	$\hat{r}$	1.6
Beta Parameter	$\hat{\beta}$	1.024
Inverse Burger Number	F	10^{-6}
Wind Forcing	$\hat{G}_{winds}$	$\frac{L\tau_0}{U^2\rho} e^{-\hat{r}^2}$

Table 4.6: The values used during implementation of the models discussed in Section 2.44 and 2.3 under the Beaufort gyre regime.

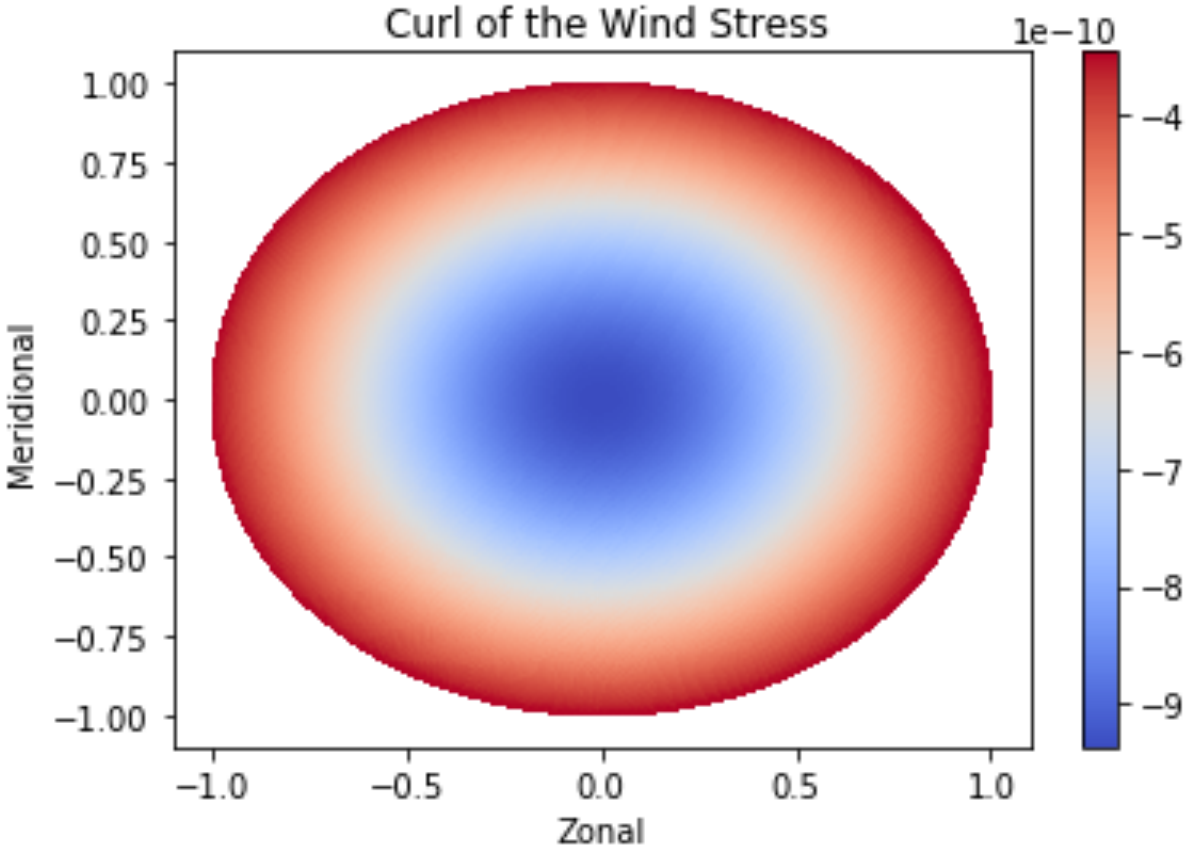

Figure 4.10: The curl of the wind stress which drives vorticity of the gyre in the Beaufort gyre regime.

remote machine, cpu141. Most solutions have been obtained using serial computing. Due to numerical instabilities and restrictions to memory during the Beaufort gyre winds were reduced by a factor of 10^{-12} during implementation.

4.2.2 Linear Steady Solutions

We begin by presenting the streamfunction solution, overlaid with velocity in Figure 4.11. This plot has been obtained by using the parameters associated with the Beaufort gyre as listed in Table 4.6. The flow follows an anti-cyclonic motion, with faster velocities in the centre of the gyre. The velocity at the centre of the gyre indicate the flow is not perfectly symmetrical, which may be attributed the small beta value. Based on studies, such as [43], we expect the small beta value to have little impact on the solution. In Figure 4.12, we present the effects of a varying beta parameter on the streamfunction and potential vorticity. In Figure 4.12a and 4.12b, we have taken a beta to be zero, leading to a radially symmetric plot. Similar to the quiver plot, the streamfunction solutions have an anti-cyclonic flow, with maximal velocities in the centre. As well, the potential vorticity reaches a minimum as the centre and zero on the boundaries. In Figure 4.12c and 4.12d, we have increase beta to be $\beta = 1.024$, the beta value associated with the Beaufort gyre. The streamfunction in 4.12c shows slight indication of asymmetry in the latitudinal direction, however the asymmetry of the potential vorticity is much more apparent. The eastern boundary obtains a value of zero, while the western boundary obtains intermediate values of negative vorticity. Finally in Figures 4.12e and 4.12f, we present the solutions for $\beta = 10.0$. This increase shows a drastic difference in the symmetry, and displays what the Beaufort gyre might look like in the sub-tropics where the beta values are larger, resulting in a western boundary current.

In Figure 4.13, we present the streamfunction and potential vorticity solutions obtained by varying the value of the Burger number, or equivalently the inverse Burger number. In all other plots presented in this section, we have taken the inverse Burger number to be $F = 10^{-6}$. In Figure 4.13, we again use a different color bar for each plot in order to present details for wide ranges of magnitudes. In Figure 4.13a and 4.13b we show the solution for $F = 0.1$ and beta has been taken to be 1.024 for the Beaufort gyre. Comparing this to the idealized Beaufort gyre solution plot in Figure 4.12d, where we have used the same beta parameter and an inverse Burger number of 10^{-6}, we do not see significant differences. As we increase to let $F = 10.0$, we see the magnitudes in the streamfunction decrease, and the potential vorticity solutions begin to look more radially symmetrical. If we increase further and take $F = 100.0$ in Figure 4.13d and 4.13e, we notice the streamfunction has reduced in magnitude further and the potential vorticity solution looks perfectly symmetric. If we

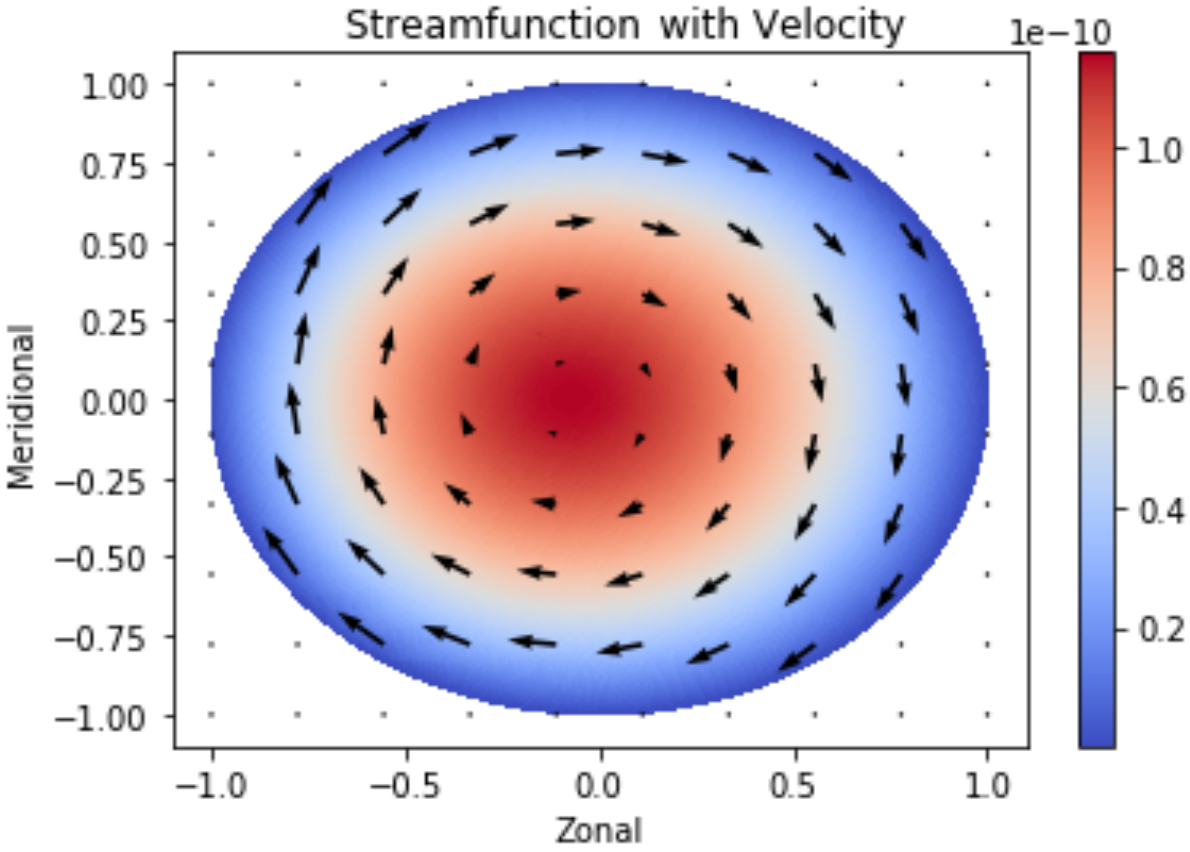

Figure 4.11: The steady linear streamfunction imposed with the velocity associated with equation 2.48 under the Beaufort gyre regime. The parameters applied are listed in Table 4.6.

were to use the inverse beta value associated with the Beaufort gyre, $F = 62.5$, we would expect to see similar results to the solutions. That is, we would expect to see increased radial symmetry and reduced streamfunction values.

4.2.3 Nonlinear, Time-Dependent Solutions

Similar to the classical regime, we show the nonlinear, time dependent solution converges to the steady solution for the Beaufort gyre regime as well. In Figure 4.14, we provide the results confirming this for the Beaufort gyre problem. Again, we have initialized the problem with zero vorticity, which results in a solution very close to the steady solution shown in Figures 4.12c and 4.12d. The streamfunction and potential vorticity solution presented in Figures 4.14c and 4.14d show how quickly the solution converges to the steady solution. The convergence was again measured using the norm of the error to an accuracy of two decimals.

In Figure 4.15 and 4.16 we present the solutions for the nonlinear perturbation evolution. The potential vorticity perturbation, Figure 4.16 resembles a similar evolution as that found in the classical regime, Figure 4.5f with perturbations obtaining maximum values along the western boundary. However, in this regime, we see the perturbations have reduced significantly, obtaining magnitudes of order 10^{-10} by $\hat{t} = 9.6$, whereas the classical regime maintained a similar magnitude for the solutions we investigated, up to $\hat{t} = 355$. The streamfunction perturbation in Figure 4.15 begins similar to the classical nonlinear perturbation evolution, with minimum values on the western boundary and absolute maximal values in the centre. However, due to numerical instabilities, we were not able to explore the nonlinear perturbation for further time steps.

4.2.4 Linear Stability Solutions

We finally look at the linear stability solutions for the Beaufort gyre regime. In Figure 4.18 we present the potential vorticity perturbation evolution and see the solutions favour the western side, as we began to see in the nonlinear perturbation of the previous section. Given the restrictions of the nonlinear model, it is hard to compare the results found here. However, we may note the westward propagating basin modes which continue indefinitely. We see the perturbation grows along the western boundary and goes to zero elsewhere. The streamfunction perturbation for the linear stability model is also difficult to compare to the nonlinear perturbation evolution given the few times steps we were able to obtain. However, the solution in Figure 4.17a look very similar to the nonlinear plot, Figures 4.15b. The

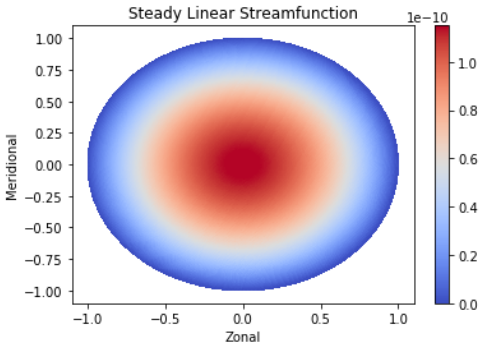

(a) $\hat{\beta} = 0.0$

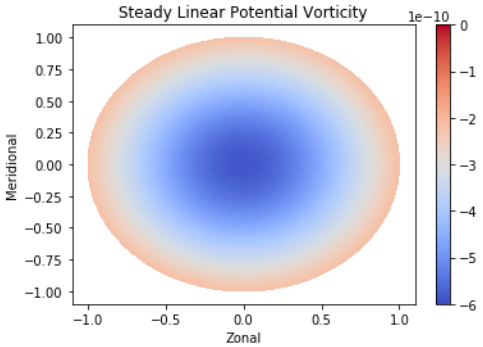

(b) $\hat{\beta} = 0.0$

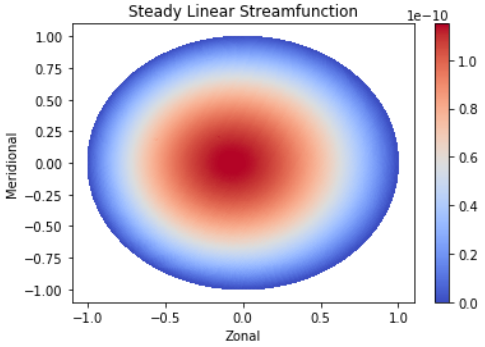

(c) $\hat{\beta} = 1.024$

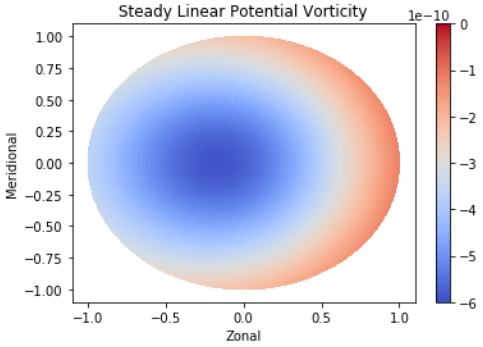

(d) $\hat{\beta} = 1.024$

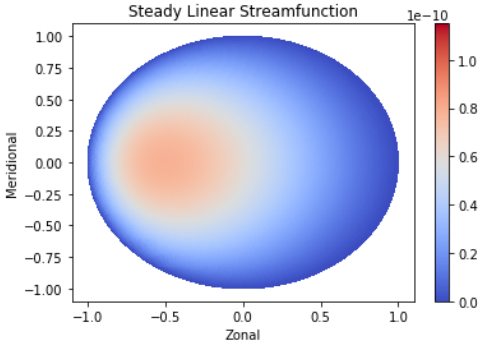

(e) $\hat{\beta} = 10.0$

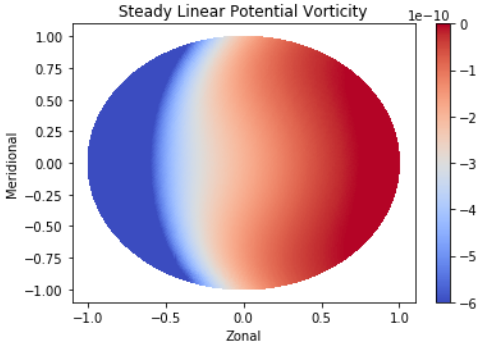

(f) $\hat{\beta} = 10.0$

Figure 4.12: The streamfunction (left) and potential vorticity (right) in the steady, linear model (2.48) in the Beaufort gyre regime, with non-dimensional beta = 0, 1.024, and 10.0 for constant inverse Burger number 10^{-6}.

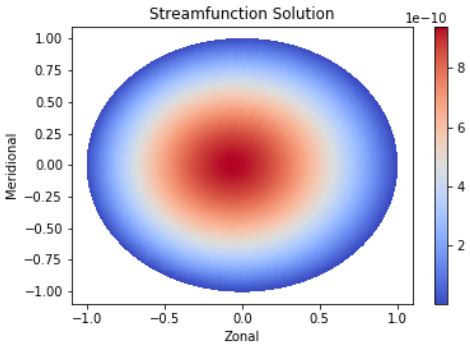

(a) F=0.1

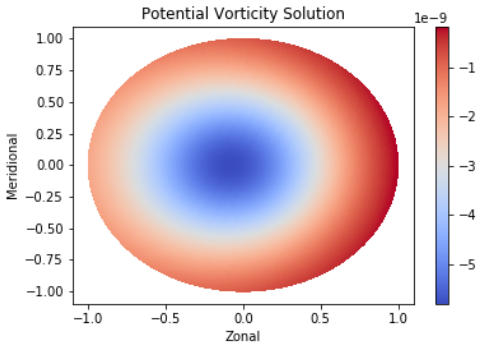

(b) F=0.1

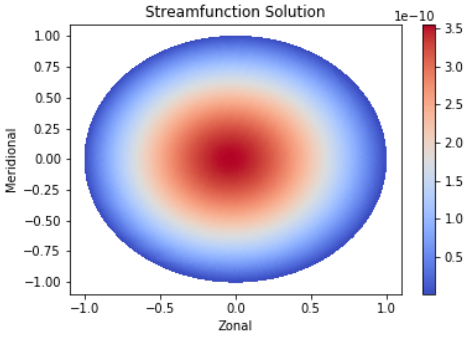

(c) F=10.0

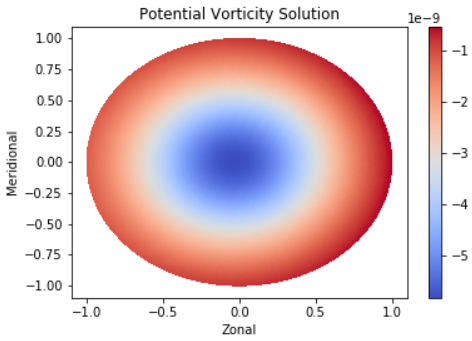

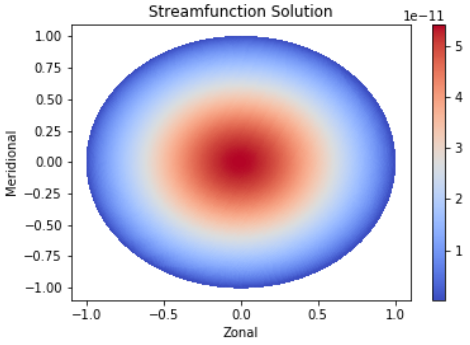

(d) F=100.0

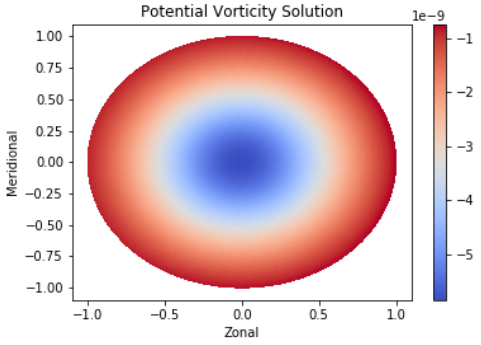

(e) F=100.0

Figure 4.13: The steady linear streamfunction (left) and potential vorticity (right) (2.48) in the Beaufort gyre regime, with inverse Burger number = 0.1 , 10.0, and 100.0 for constant non-dimensional beta 1.024. Due to the wide range of values, each figure has an individual color bar.

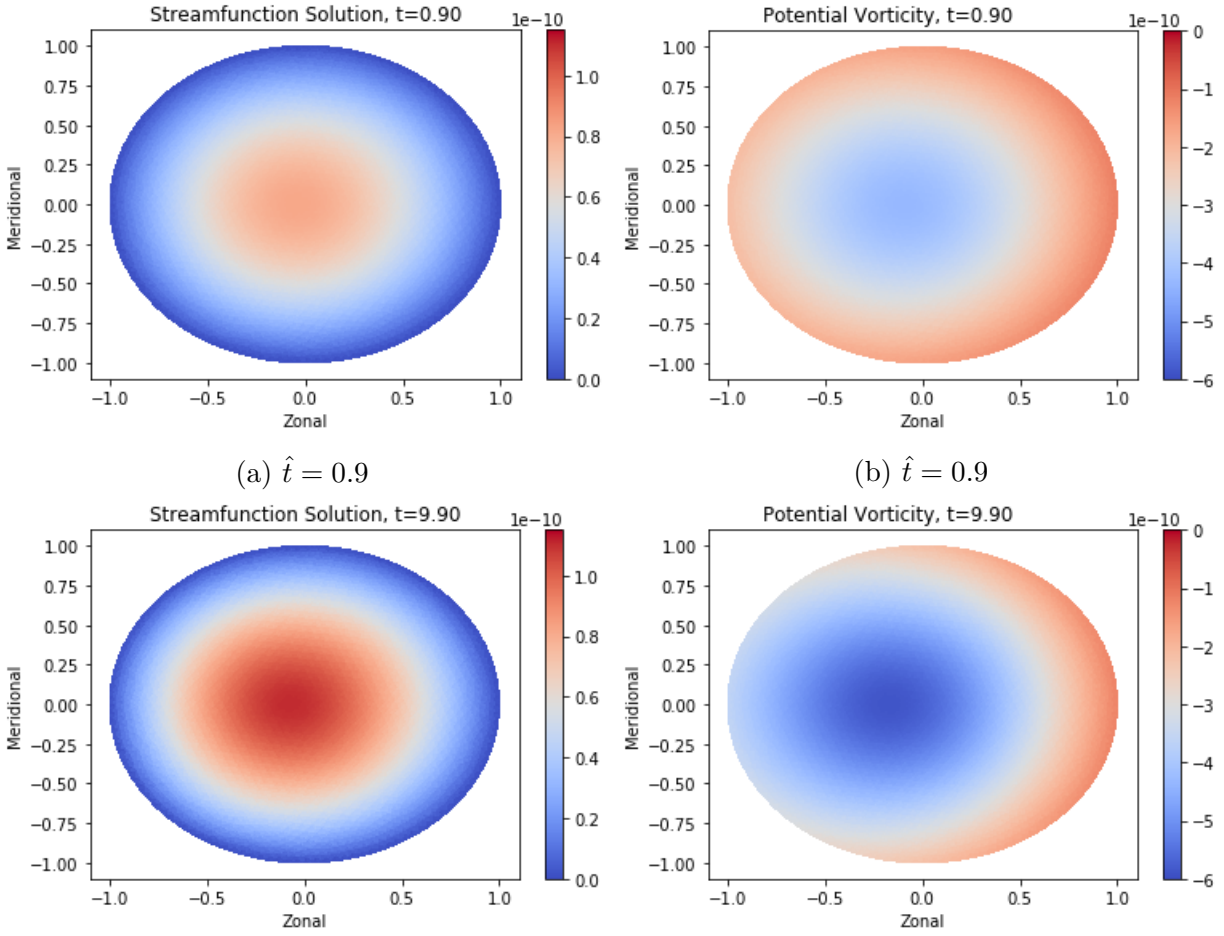

(a) $\hat{t} = 0.9$

(b) $\hat{t} = 0.9$

(c) $\hat{t} = 9.90$

(d) $\hat{t} = 9.90$

Figure 4.14: The streamfunction (left) and the potential vorticity (right) in the nonlinear, time dependent model (2.44) in the Beaufort gyre regime, initialized with zero potential vorticity. These solutions evolved until converged to the steady solution as seen in Figure 4.11.

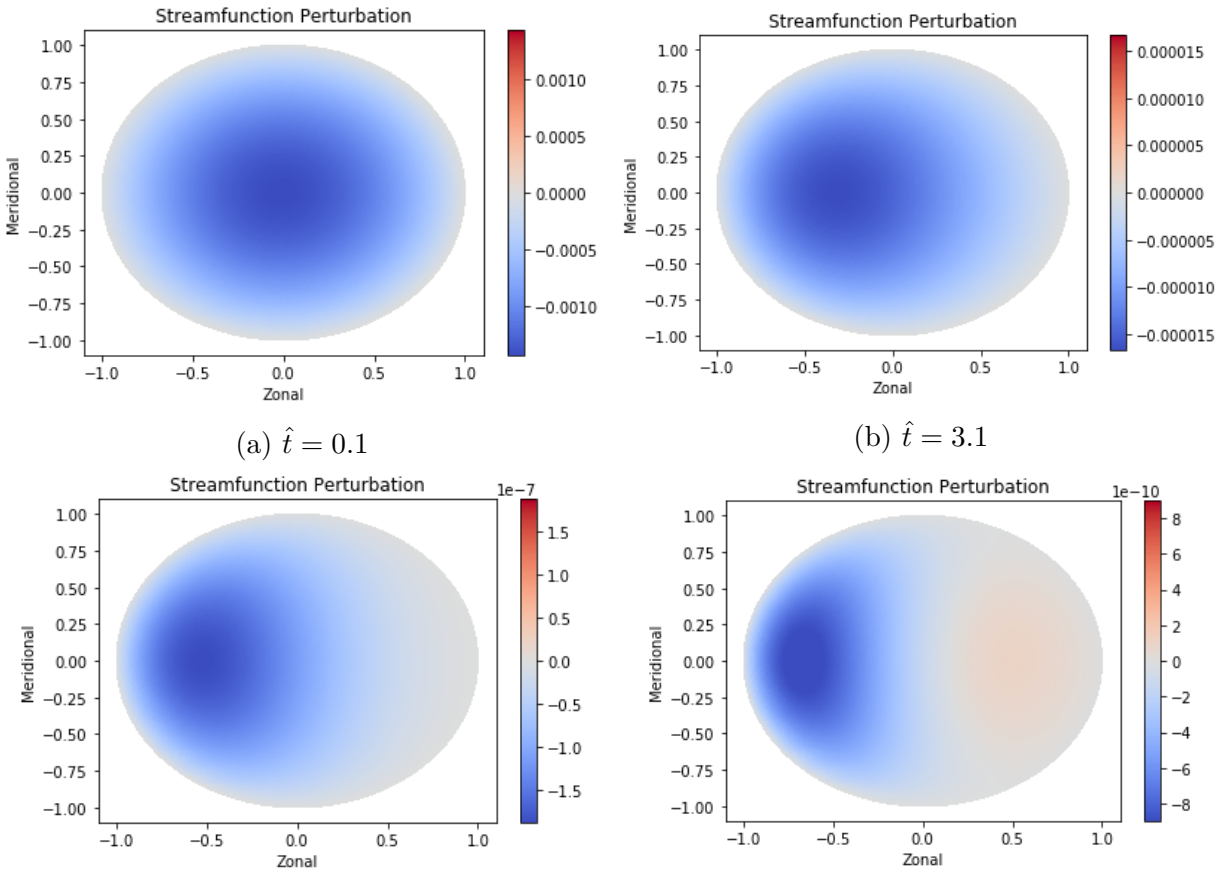

(a) $\hat{t} = 0.1$

(b) $\hat{t} = 3.1$

(c) $\hat{t} = 6.1$

(d) $\hat{t} = 9.6$

Figure 4.15: The streamfunction perturbation in the nonlinear, time dependent model (2.44) in the Beaufort gyre regime. These solutions have been initialized with a perturbed basic state, and these solutions show how the perturbations grow in time. The associated potential vorticity is seen in Figure 4.16.

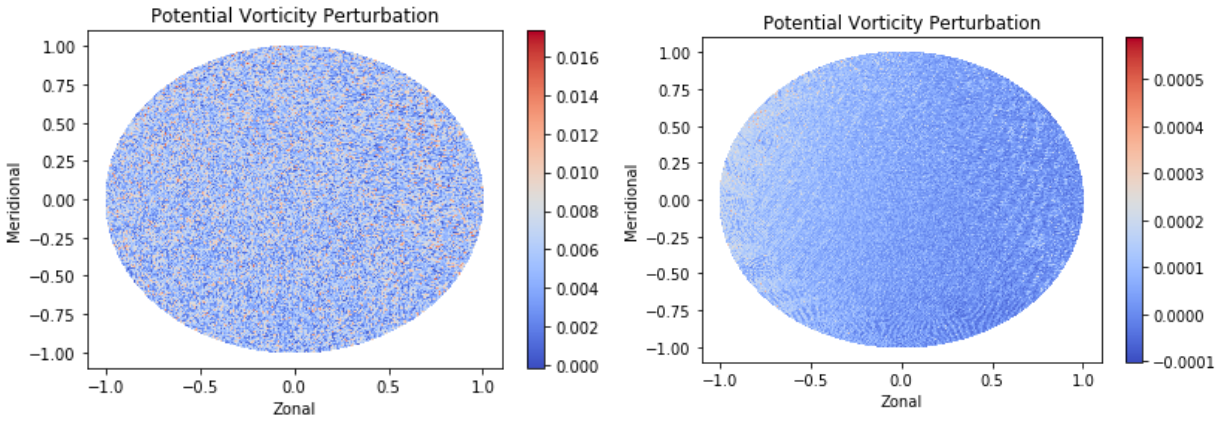

(a) $\hat{t} = 0.1$

(b) $\hat{t} = 3.1$

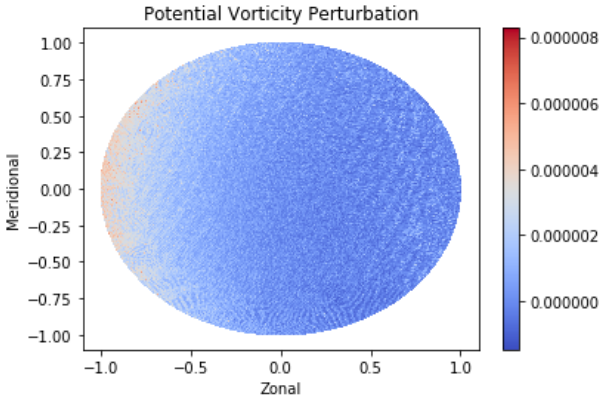

(c) $\hat{t} = 6.1$

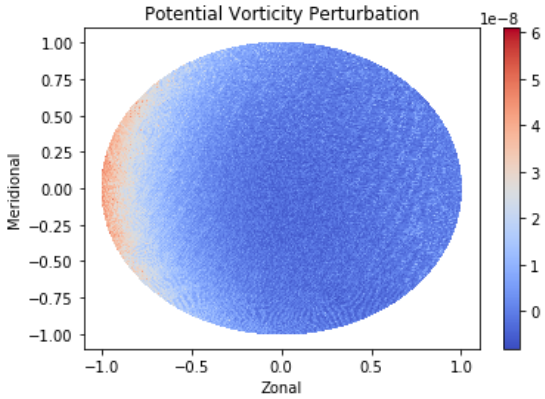

(d) $\hat{t} = 9.6$

Figure 4.16: The potential vorticity perturbation in the nonlinear, time dependent model (2.44) in the Beaufort gyre regime. These solutions have been initialized with a perturbed basic state and these solutions show how the perturbations evolve in time. The associated streamfunction is seen in Figure 4.15.

linear stability solution continues to propagate basin modes towards the western boundary indefinitely.

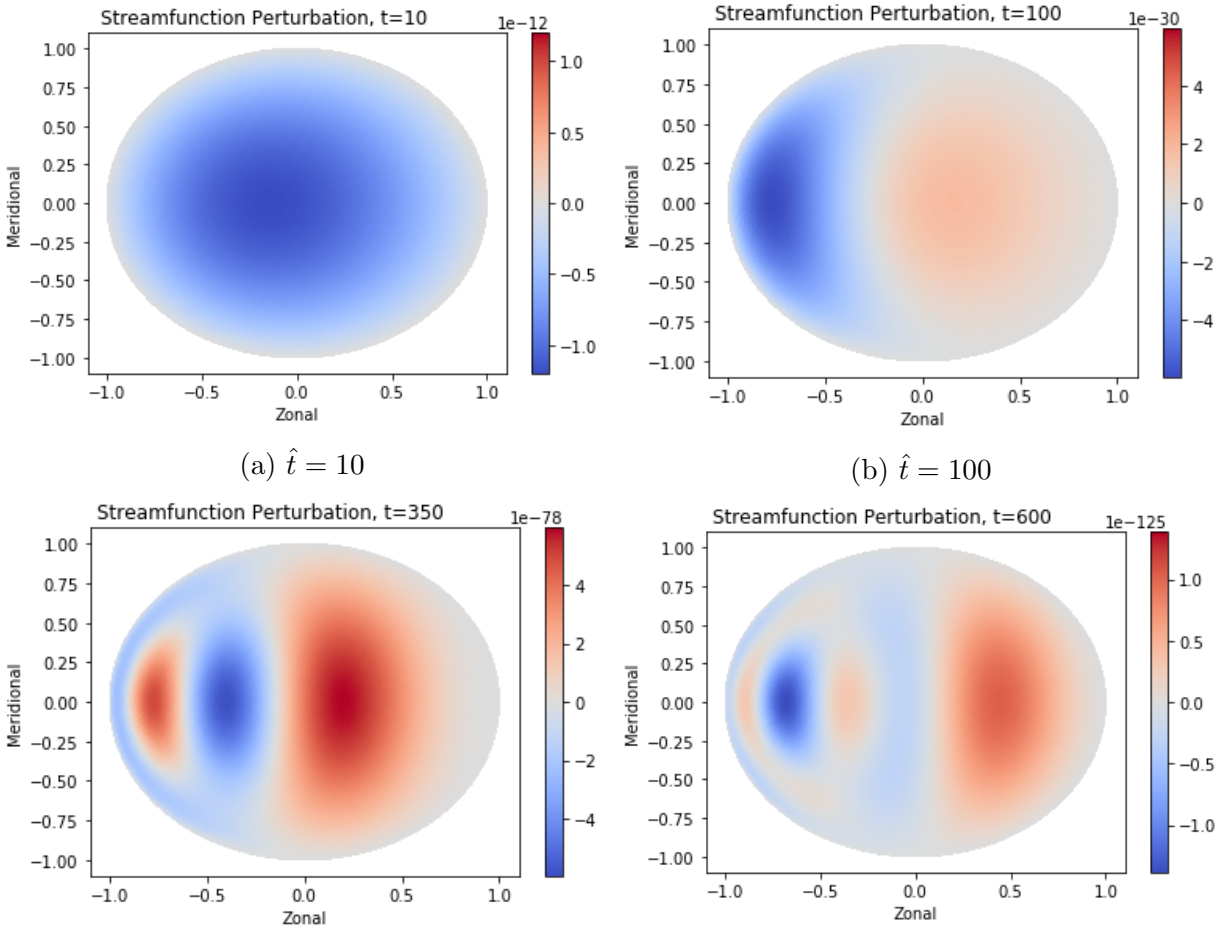

(a) $\hat{t} = 10$

(b) $\hat{t} = 100$

(c) $\hat{t} = 350$

(d) $\hat{t} = 600$

Figure 4.17: The streamfunction perturbation in the linear stability model (2.68) in the Beaufort gyre regime. These solutions have been initialized with a perturbation for potential vorticity and show how the streamfunction perturbations change in time. The associated potential vorticity is seen in Figure 4.18.

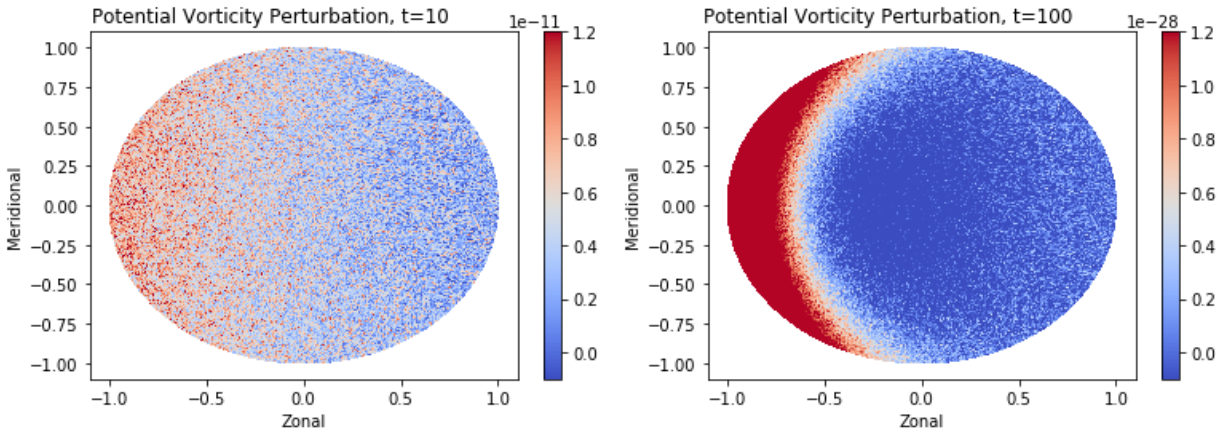

(a) $\hat{t} = 10$

(b) $\hat{t} = 100$

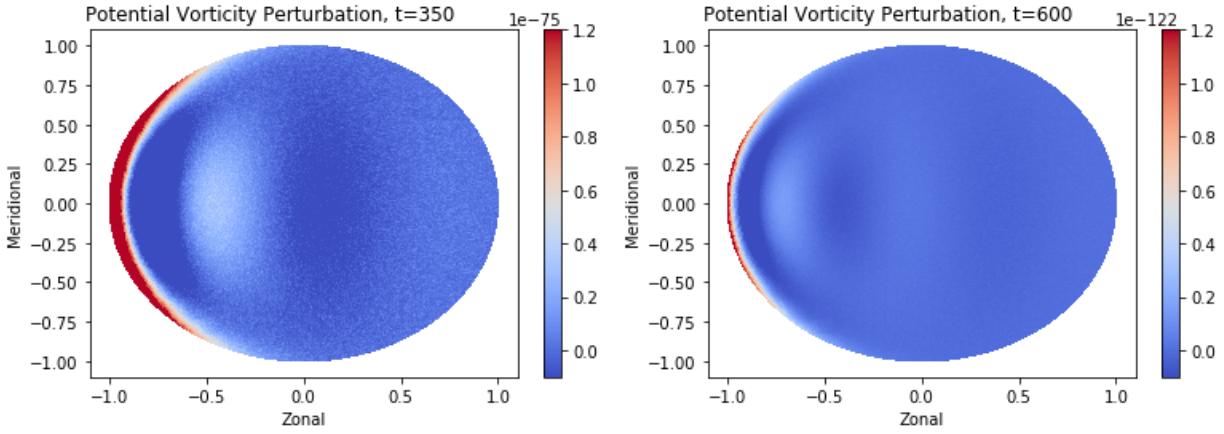

(c) $\hat{t} = 350$

(d) $\hat{t} = 600$

Figure 4.18: The potential vorticity perturbation in the linear stability model (2.68) in the Beaufort gyre regime. These solutions have been initialized with a perturbation for potential vorticity and show how the perturbations evolve in time. The associated stream-function is seen in Figure 4.17

Chapter 5

Conclusions

The work done in this thesis aimed to better understand the spatial structure of the Beaufort gyre and to identify instabilities within the system. In order to do this, tools were developed to study two very different gyres in the context of a one-layer, reduced-gravity, QG model. We used the results from [30] and [17] to guide the development of the tools for a gyre in a square domain.

The first tool computes the steady linear wind-driven gyre solution and provides an answer to the first research question. For the Beaufort gyre regime, a circular wind led to a spatial structure that greatly depended on the model parameters. Using this tool, we investigated how the spatial structure of the solution depends on the bottom drag, the beta parameter, and the Burger number. With a very small Burger number or a very small beta value, the steady solution was symmetrical in both the longitudinal and latitudinal directions, with little to no western intensification. In all other cases, the solutions showed varying asymmetry in longitude, with the western boundary having the sharpest variations in the streamfunction and therefore the strongest velocities. As well, the potential vorticity displayed stronger asymmetries than the associated streamfunction solutions. This result held true for two different wind forcing patterns, as well as different geometries. Yang et. al (2016) performed similar experiments to investigate the β effect on the Beaufort gyre [43]. They used a two-layer, nonlinear wind-driven gyre model for an idealized circular domain, and also considered bottom drag and lateral viscosity. As well, Yang et. al (2016) used an anti-cyclonic wind stress curl, however used a sloping bathymetry with a flat bottom in the centre of the domain. They investigated the affects of different β for a circular domain, and in a circular domain which has has the western edge shortened to introduce a western boundary. The results suggest the model solution is more sensitive to the changes in the domain with a western boundary. This suggests we might have

seen more significant asymmetries if we had imposed a western boundary in the domain. This first step provided some insights into how to the spatial structure of the wind-driven gyre depends on the parameters. Often this problem is solved using asymptotically using boundary layer methods, but this tool allows for us to compute solutions that are more accurate.

The second tool was used to model the nonlinear evolution of a wind-driven gyre and was used in two ways. The first was to validate the steady solver mentioned above, by showing that the nonlinear solutions converged to the steady solution within a reasonable order of accuracy, which was measured using the norm. That is to say, the first tool and the second tool were tested to ensure they produced the same result, and showed the steady solution is asymptotically stable. The second purpose of the tool was to simulate the evolution of a perturbed wind-driven gyre solution by adding small perturbations to the basic state. In both cases the potential vorticity perturbations reached maximum values along the western boundary, regardless of the actual thickness of the western boundary current obtained in the steady solution. In the perturbed case, the streamfunction solution for the nonlinear evolution model displayed basin mode propagation towards the western boundary and rode on the wind-driven gyre. These basin modes seemed to continue indefinitely but it was observed that their amplitudes did decay in time. For the Beaufort gyre regime, the streamfunction solutions began to change similar to the start of the classical regime, however numerical divergence issues prevented us from exploring the solutions for stronger winds than what we considered here. The reduction of the winds have great impact on the overall results. By reducing the magnitude of the wind stress curl, we not only reduced the practicality of the model, we also reduced the importance of the nonlinear terms. Using a weak wind regime led to a minuscule difference between the nonlinear and linear problem, and thus the nonlinear model behaved more like a linear model. Although this defeats the purpose of a nonlinear model, it does however allow for the usage of the linear steady model as the basic state solution in the stability model. When analyzing the stability of a solution, the exact solution should be used for the basic state. Exact solutions are hard to come by for the problem we are analyzing, and a computational solution has therefore been used.

The final tool was developed to identify and analyze instabilities using a linear stability model. It was expected to produce similar results as the nonlinear simulations in the case where the perturbations were sufficiently small compared to the magnitude of the basic state. Interestingly, it was noted that magnitudes of the stability solutions reduced quickly, while the magnitudes of the nonlinear solutions remained nearly constant, suggesting the nonlinear model experiences weaker dissipation. As well, in both the classical and the Beaufort gyre regimes, the potential vorticity perturbation was localized along the western

boundary, again regardless of the calculated western boundary thickness. The streamfunction for both regimes produced westward propagating basin modes. Unfortunately, we were unable to simulate instabilities in either of the gyres we considered. The western boundary currents were too thick, or the winds are too weak, to generate strong enough jets that would lead to the destabilization of the basin modes. However, for the Beaufort gyre regime, the amplitudes of the perturbations continued to reduce in size, answering our second research question: the Beaufort gyre is stable under the applied wind regime. The work done by [30] and [17] provided some guidance as to where to look in parameter space for instabilities under the classical regime, but the numerical model was unable to converge, thus preventing a thorough exploration of the regime. This leads us to the discussion of future directions in order to simulate instabilities, and to improve the model.

The work accomplished in this thesis provides a tool kit for future instability analysis of a wind-driven gyre. We present three ways in which this work may be added to, or improved upon. Firstly, further tests should be done in order to thoroughly search for instabilities in a regime where the western boundary current is much narrower. Second, the numerical methods may be improved upon in terms of accuracy and robustness. This may be done by using a finer mesh, and using a higher order finite element and time-stepping methods, such as Crank Nicolson. Thirdly, in order to more accurately represent the Beaufort gyre, it may be useful to consider the interaction between the freshwater layer and the salty layer below, as well as the interaction between the fresh water layer and the floating sea ice. The simulation results presented in this thesis used an inverse Burger number of 10^{-6}. This is a near rigid lid approximation, and may be useful to also consider the completely free surface case, given the fact that the Arctic is nearing a state of no ice. As the arctic environment continues to change, understanding the Beaufort gyre stability becomes more and more important. Although we were not able to identify instabilities in the system, we were able to study the evolution of the perturbed gyre. The work done here hopes to lead to further understanding and bring attention to the importance of the Beaufort gyre.

References

[1] Thomas W K Armitage, Georgy E Manucharyan, Alek A Petty, Ron Kwok, and Andrew F Thompson. Enhanced eddy activity in the Beaufort Gyre. *Nature Communications*, 11(761):1–8, 2020.

[2] Igor M. Belkin. Propagation of the "Great Salinity Anomaly" of the 1990s around the northern North Atlantic. *Geophysical Research Letters*, 31(8):4–7, 2004.

[3] Jane B Blizard. Angular momentum. In *Encyclopedia of Planetary Science*, pages 12–13. Springer Netherlands, Dordrecht, 1997.

[4] E. C. Carmack, M. Yamamoto-Kawai, T. W.N. Haine, S. Bacon, B. A. Bluhm, C. Lique, H. Melling, I. V. Polyakov, F. Straneo, M. L. Timmermans, and W. J. Williams. Freshwater and its role in the Arctic Marine System: Sources, disposition, storage, export, and physical and biogeochemical consequences in the Arctic and global oceans. *Journal of Geophysical Research G: Biogeosciences*, 121(3):675–717, 2016.

[5] Benoit Cushman-Roisin and Jean-Marie Beckers. Introduction to Geophysical Fluid Dynamics. Physical and Numerical Aspects. *Analysis*, 101:786, 2010.

[6] Peter E.D. Davis, Camille Lique, and Helen L. Johnson. On the link between arctic sea ice decline and the freshwater content of the beaufort gyre: Insights from a simple process model. *Journal of Climate*, 27(21):8170–8184, 2014.

[7] Robert R. Dickson, Jens Meincke, Svend Aage Malmberg, and Arthur J. Lee. The "great salinity anomaly" in the Northern North Atlantic 1968-1982. *Progress in Oceanography*, 20(2):103–151, 1988.

[8] Edward W. Doddridge, Gianluca Meneghello, John Marshall, Jeffery Scott, and Camille Lique. A Three-Way Balance in the Beaufort Gyre: The Ice-Ocean Gov-

ernor, Wind Stress, and Eddy Diffusivity. *Journal of Geophysical Research: Oceans*, 124(5):3107–3124, 2019.

[9] Glenn Elert and Jason Atkins. The Physics Fact Book, 2002.

[10] Firedrake. Firedrake Library, an automated finite element system, 2016.

[11] Baylor Fox-Kemper. Eddies and friction : removal of vorticity from the wind-driven gyre. *Eddies and friction : removal of vorticity from the wind-driven gyre*, 2003.

[12] Matheus Grasselli and Dmitry Pelinovsky. *Numerical Mathematics*. Jones & Bartlett Learning, 2007.

[13] H. Haak, J. Jungclaus, U. Mikolajewicz, and M. Latif. Formation and propagation of great salinity anomalies. *Geophysical Research Letters*, 30(9):10–13, 2003.

[14] G. R. Ierley and V. A. Sheremet. Multiple solutions and advection-dominated flows in the wind-driven circulation. Part I: slip. *Journal of Marine Research*, 53(5):703–737, 1995.

[15] Woods Hole Oceanographic Insitution. Beaufort Gyre Exploration Project, 2014.

[16] Lakshmi H Kantha and Carol Anne Clayson. Small Scale Processes in Geophysical Fluid Flows. In *Small Scale Processes in Geophysical Fluid Flows*, pages 172–173. Academic Press, 1 edition, 2000.

[17] William Ko. *High-Resolution Numerical Simulations of Barotropic Wind-Driven Gyres*. PhD thesis, University of Waterloo, 2011.

[18] Igor E. Kozlov, Anastasia V. Artamonova, Georgy E. Manucharyan, and Arseny A. Kubryakov. Eddies in the Western Arctic Ocean From Spaceborne SAR Observations Over Open Ocean and Marginal Ice Zones. *Journal of Geophysical Research: Oceans*, 124(9):6601–6616, 2019.

[19] Pijush K. Kundu and Ira M. Cohen. *Fluid Mechanics*. Academic Press, 2 edition, 2002.

[20] J. H. LaCasce and J. Pedlosky. The instability of Rossby basin modes and the oceanic eddy field. *Journal of Physical Oceanography*, 34(9):2027–2041, 2004.

[21] Maria V Luneva, Andrew J Willmott, Miguel Angel, and Morales Maqueda. Geostrophic Adjustment Problems in a Polar Basin. *Atmosphere-Ocean*, 5900, 2012.

[22] Georgy E Manucharyan and Michael A Spall. Wind-driven freshwater buildup and release in the Beaufort Gyre constrained by mesoscale eddies. *Geophysical Research Letters*, 43(1):273–282, 2016.

[23] Georgy E Manucharyan, Michael A Spall, and Andrew F Thompson. A Theory of the Wind-Driven Beaufort Gyre Variability. *Journal of Physical Oceanography*, 46:3263–3278, 2016.

[24] Torge Martin, Michael Steele, and Jinlun Zhang. Seasonality and long-term trend of Arctic Ocean surface stress in a model. *Journal of Geophysical Research : Oceans*, 119(3):3909–3925, 2014.

[25] Gianluca Meneghello, John Marshall, Jean Michel Campin, Edward Doddridge, and Mary Louise Timmermans. The Ice-Ocean Governor: Ice-Ocean Stress Feedback Limits Beaufort Gyre Spin-Up. *Geophysical Research Letters*, 45(20):293–11, 2018.

[26] Gianluca Meneghello, John Marshall, Mary Louise Timmermans, and Jeffery Scott. Observations of seasonal upwelling and downwelling in the Beaufort Sea mediated by sea ice. *Journal of Physical Oceanography*, 48(4):795–805, 2018.

[27] Adam Morgan. *Finite Element Exterior Calculus with Applications to the Numerical Solution of the Green-Naghdi Equations*. PhD thesis, University of Waterloo, 2018.

[28] Walter H. Munk. On The Wind-Driven Ocean Circulation. *Journal of Meteorology*, 7(2):79–93, 1950.

[29] Joseph Pedlosky and Michael A. Spall. Boundary Intensification of Vertical Velocity in a β -Plane Basin. *Journal of Physical Oceanography*, 35(12):2487–2500, 2006.

[30] Francis Poulin, William Ko, Baylor Fox-Kemper, and N.K.R. Kevlahan. Spectral and Ageostrophic Characteristics of Turbulent Wind-Driven Gyre Flow Manuscript. 0.

[31] Andrey Proshutinsky, Richard Krishfield, Mary-Louise Timmermans, John Toole, Eddy Carmack, Fiona McLaughlin, William J. Williams, Sarah Zimmermann, Motoyo Itoh, and Koji Shimada. Beaufort Gyre freshwater reservoir: State and variability from observations. *Journal of Geophysical Research*, 114:1–25, 2009.

[32] Andrey Proshutinsky, Richard Krishfield, J.M Toole, Mary Louise Timmermans, W Williams, S Zimmermann, M Yamamoto-Kawai, Thomas W Armitage, D Dukshovskoy, E Golubeva, Georgy E Manucharyan, G Platov, E Watanabe, T Kikuchi, S Nishino, M Itoh, S-H Kang, K-H Cho, K Tateyama, and J Zhao. Analysis of the

Beaufort Gyre Freshwater Content in 2003 – 2018. *ournal of Geophysical Research : Oceans*, 124:9658–9689, 2019.

[33] Heather C. Regan, Camille Lique, and Thomas W.K. Armitage. The Beaufort Gyre Extent, Shape, and Location Between 2003 and 2014 From Satellite Observations. *Journal of Geophysical Research: Oceans*, 124(2):844–862, 2019.

[34] Raymond A. Serway and Jr. John W. Jewett. *Physics for Scientists and Engineers with Modern Physics*. Cengage Learning, ninth edit edition, 2016.

[35] V. A. Sheremet, G. R. Ierley, and V. M. Kamenkovich. Eigenanalysis of the two-dimensional wind-driven ocean circulation problem. *Journal of Marine Research*, 55(1):57–92, 1997.

[36] Michael A. Spall. On the circulation of Atlantic water in the Arctic Ocean. *Journal of Physical Oceanography*, 43(11):2352–2371, 2013.

[37] Henry Stommel. The Western Intensification of Wind-Driven Ocean Currents. *American Geophysical Union*, 29(2):202–206, 1948.

[38] Mary Louise Timmermans. Personal Email, 2019.

[39] Mary Louise Timmermans and John Marshall. Understanding Arctic Ocean Circulation: A Review of Ocean Dynamics in a Changing Climate. *Journal of Geophysical Research: Oceans*, 125(4):1–35, 2020.

[40] Mary Louise Timmermans, H. Melling, and L. Rainville. Dynamics in the deep Canada Basin, Arctic Ocean, inferred by thermistor chain time series. *Journal of Physical Oceanography*, 37(4):1066–1076, 2007.

[41] Geoffrey K. Vallis. *Atmospheric and Oceanic Fluid Dynamics*. Cambridge University Press, 2005.

[42] Woods Hole Oceanographic Institution. Beaufort Gyre Publications, 2020.

[43] Jiayan Yang, Andrey Proshutinsky, and Xiaopei Lin. Dynamics of an idealized Beaufort Gyre: 1. the effect of a small beta and lack of western boundaries. *Journal of Geophysical Research: Oceans*, 121(2):1249–1261, 2016.

[44] Jinlun Zhang, Michael Steele, Kay Runciman, Sarah Dewey, James Morison, Craig Lee, Luc Rainville, Sylvia Cole, Richard Krishfield, Mary-Louise Timmermans, and John Toole. The Beaufort Gyre intensification and stabilization: A model- observation synthesis. *Journal of Geophysical Research: Oceans*, 122:2647–2651, 2017.